

Stellar laboratories

VII. New Kr IV – VII oscillator strengths and an improved spectral analysis of the hot, hydrogen-deficient DO-type white dwarf RE 0503–289^{★, ★★, ★★★, ★★★★★, †}

T. Rauch¹, P. Quinet^{2,3}, D. Hoyer¹, K. Werner¹, P. Richter^{4,5}, J. W. Kruk⁶, and M. Demleitner⁷

¹ Institute for Astronomy and Astrophysics, Kepler Center for Astro and Particle Physics, Eberhard Karls University, Sand 1, 72076 Tübingen, Germany

e-mail: rauch@astro.uni-tuebingen.de

² Physique Atomique et Astrophysique, Université de Mons – UMONS, 7000 Mons, Belgium

³ IPNAS, Université de Liège, Sart Tilman, 4000 Liège, Belgium

⁴ Institute of Physics and Astronomy, University of Potsdam, Karl-Liebknecht-Str. 24/25, 14476 Golm, Germany

⁵ Leibniz-Institut für Astrophysik Potsdam (AIP), An der Sternwarte 16, 14482 Potsdam, Germany

⁶ NASA Goddard Space Flight Center, Greenbelt, MD 20771, USA

⁷ Astronomisches Rechen-Institut (ARI), Centre for Astronomy of Heidelberg University, Mönchhofstraße 12-14, 69120 Heidelberg, Germany

Received 14 January 2016; accepted 22 February 2016

ABSTRACT

Context. For the spectral analysis of high-resolution and high signal-to-noise (S/N) spectra of hot stars, state-of-the-art non-local thermodynamic equilibrium (NLTE) model atmospheres are mandatory. These are strongly dependent on the reliability of the atomic data that is used for their calculation.

Aims. New Kr IV–VII oscillator strengths for a large number of lines enable us to construct more detailed model atoms for our NLTE model-atmosphere calculations. This enables us to search for additional Kr lines in observed spectra and to improve Kr abundance determinations.

Methods. We calculated Kr IV–VII oscillator strengths to consider radiative and collisional bound-bound transitions in detail in our NLTE stellar-atmosphere models for the analysis of Kr lines that are exhibited in high-resolution and high S/N ultraviolet (UV) observations of the hot white dwarf RE 0503–289.

Results. We reanalyzed the effective temperature and surface gravity and determined $T_{\text{eff}} = 70\,000 \pm 2000$ K and $\log(g / \text{cm s}^{-2}) = 7.5 \pm 0.1$. We newly identified ten Kr V lines and one Kr VI line in the spectrum of RE 0503–289. We measured a Kr abundance of -3.3 ± 0.3 (logarithmic mass fraction). We discovered that the interstellar absorption toward RE 0503–289 has a multi-velocity structure within a radial-velocity interval of $-40 \text{ km s}^{-1} < v_{\text{rad}} < +18 \text{ km s}^{-1}$.

Conclusions. Reliable measurements and calculations of atomic data are a prerequisite for state-of-the-art NLTE stellar-atmosphere modeling. Observed Kr V–VII line profiles in the UV spectrum of the white dwarf RE 0503–289 were simultaneously well reproduced with our newly calculated oscillator strengths.

Key words. atomic data – line: identification – stars: abundances – stars: individual: RE 0503–289 – stars: individual: RE 0457–281 – virtual observatory tools

1. Introduction

Reliably determining the abundance of trans-iron elements in hot white dwarf (WD) stars, e.g., G191–B2B and RE 0503–289 (WD 0501+527 and WD 0501–289, respectively), McCook & Sion 1999a,b), recently became possible with the calculation of transition probabilities for highly ionized Zn (atomic number $Z = 30$), Ga (31), Ge (32), Mo (42), and Ba (56) (Rauch et al. 2014a, 2015b, 2012, 2015a, 2014b). These analyses were initiated by the discovery of lines of Ga, Ge, As (33), Se (34), Kr (36), Mo, Sn (50), Te (52), I, (53), and Xe (54) in the Far Ultraviolet Spectroscopic Explorer (FUSE) spectrum of the hydrogen-deficient DO-type WD RE 0503–289 by Werner et al. (2012b). Owing to the lack of atomic data at that time, they could only measure the Kr and Xe abundances (-4.3 ± 0.5 and -4.2 ± 0.6 in logarithmic mass fractions, respectively). We calculated new Kr IV–VII transition probabilities to

[★] Based on observations with the NASA/ESA *Hubble* Space Telescope, obtained at the Space Telescope Science Institute, which is operated by the Association of Universities for Research in Astronomy, Inc., under NASA contract NAS5-26666.

^{★★} Based on observations made with the NASA-CNES-CSA Far Ultraviolet Spectroscopic Explorer.

^{★★★} Based on observations made with ESO Telescopes at the La Silla Paranal Observatory under programme IDs 165.H-0588 and 167.D-0407.

^{★★★★} Based on observations obtained at the German-Spanish Astronomical Center, Calar Alto, operated by the Max-Planck-Institut für Astronomie Heidelberg jointly with the Spanish National Commission for Astronomy.

[†] Tables 10 to 13 are only available via the German Astrophysical Virtual Observatory (GAVO) service TOSS (<http://dc.g-vo.org/TOSS>).

construct more detailed model atoms that are used in our non-local thermodynamical equilibrium (NLTE) model-atmosphere calculations to improve the Kr abundance determination.

In Sects. 2 and 3, we briefly describe the available observations, our model-atmosphere code, and the atomic data. Details of the transition-probability calculations and a comparison of the results with literature values are given in Sect. 4. Based on our state-of-the-art NLTE models, we start our spectral analysis with a verification of the previous determination of the effective temperature and surface gravity by Dreizler & Werner (1996, $T_{\text{eff}} = 70\,000\text{ K}$, $\log(g/\text{cm s}^{-2}) = 7.5$) in Sect. 5. An improved Kr abundance analysis for RE 0503–289 is then presented in Sect. 6. The stellar mass and the distance of RE 0503–289 are revisited in Sect. 7. At the end (Sect. 8), we take a look at the velocity field of the observed interstellar line absorption and compare it with that of the nearby hydrogen-rich, DA-type WD RE 0457–281 (WD 0455–282, $m_V = 13.90$ McCook & Sion 1999a,b; Gianninas et al. 2011). We summarize and conclude in Sect. 9.

2. Observations

We analyzed ultraviolet (UV) FUSE (described in detail by Werner et al. 2012b) and HST/STIS (*Hubble Space Telescope* / *Space Telescope Imaging Spectrograph*) observations ($1144\text{ Å} < \lambda < 3073\text{ Å}$) of RE 0503–289, that were performed on 2014 08 14. The latter spectrum was co-added from two observations with grating E140M (exposure times 2493 s and 3001 s, $1144\text{ Å} - 1709\text{ Å}$, resolving power $R \approx 45\,800$), and two observations with grating E230M (1338 s, $1690\text{ Å} - 2366\text{ Å}$ and 1338 s, $2277\text{ Å} - 3073\text{ Å}$, $R \approx 30\,000$). These STIS observations are retrievable from the Barbara A. Mikulski Archive for Space Telescopes (MAST).

In addition to the UV observations, we used optical spectra that were obtained at the European Southern Observatory (ESO) and the Calar Alto (CA) observatory. In the framework of the Supernova Ia Progenitor Survey project (SPY, Napiwotzki et al. 2001, 2003), observations were performed on 2000 09 09 and 2001 04 08 with the Ultraviolet and Visual Echelle Spectrograph (UVES) attached to the Very Large Telescope (VLT) located at ESO. The co-added spectra cover the wavelength intervals $[3290\text{ Å}, 4524\text{ Å}]$, $[4604\text{ Å}, 5609\text{ Å}]$, and $[5673\text{ Å}, 6641\text{ Å}]$ with a resolution of about 0.2 Å . Two spectra $[4094\text{ Å}, 4994\text{ Å}]$ and $[5680\text{ Å}, 6776\text{ Å}]$ were taken with the Cassegrain TWIN Spectrograph that was attached to the 3.5 m telescope at the CA observatory. Their resolution is about 3 Å (the same spectra were used by Dreizler & Werner 1996).

For RE 0457–281, we used FUSE spectra (ObsIds P1041101000, P1041102000, and P1041103000 from 2000 02 03, 2000 02 04, and 2000 02 07, respectively, with a total observation time of 47 465 s) that were obtained with the medium-resolution (MDRS) aperture. In addition, we used an IUE (International Ultraviolet Explorer) spectrum ($[1153\text{ Å}, 1947\text{ Å}]$) that was co-added from four observations that were obtained in high-resolution ($R \approx 10\,000$) mode with the large aperture (Data Ids SWP46302, SWP56213, SWP56262, and SWP56267 from 1992-11-19, 1995-11-18, 1995-12-02, and 1995-12-04, respectively, with a total exposure time of 168 360 s, Holberg et al. 1998). This is available via the MAST High-Level Science Products.

If not otherwise explicitly mentioned, all synthetic spectra shown in this paper, which are compared with an observation, are convolved with a Gaussian to model the respective re-

Table 1. Statistics of Kr IV - VII atomic levels and line transitions from Tables 10-13, respectively.

Ion	Atomic levels	Lines	Super levels	Super lines
IV	83	911	7	19
V	64	553	7	16
VI	69	843	7	19
VII	70	743	7	21
	286	3050	28	75

solving power. The observed spectra are shifted to rest wavelengths according to our measurement of the radial velocity $v_{\text{rad}} = 25.5\text{ km s}^{-1}$.

3. Model atmospheres and atomic data

We calculated plane-parallel, chemically homogeneous model-atmospheres in hydrostatic and radiative equilibrium with our Tübingen NLTE Model Atmosphere Package (TMAP¹, Werner et al. 2003, 2012a). Model atoms were provided by the Tübingen Model Atom Database (TMAD², Rauch & Deetjen 2003). TMAD was constructed as part of the Tübingen contribution to the German Astrophysical Virtual Observatory (GAVO³).

Our Kr model atom was designed with a statistical method (similar to Rauch et al. 2015b) by calculating the so-called super levels and super lines with our Iron Opacity and Interface (IrOnIc⁴, Rauch & Deetjen 2003). Using our approach, we neglected spin system and parity of the individual levels in the calculation of the super levels. This is justified because, in the atmosphere of RE 0503–289, the deviation of the levels' occupation numbers from LTE is small in the line-forming region of the atmosphere. The detailed fits of our theoretical line profiles to the observations (Sect. 6) do not give any hint of inconsistencies. To process our new Kr data, we transferred it into Kurucz's format⁵, which is readable by IrOnIc. The statistics of our Kr model atom are summarized in Table 1.

For the calculation of cross-sections, we followed Rauch & Deetjen (2003) for the transition types

- collisional bound-bound: van Regemorter (1962) formula for known f-values and an approximate formula for unknown f-values,
- radiative bound-bound: approximate formula by Cowley (1970, 1971) for the quadratic Stark effect, and
- collisional and radiative bound-free: Seaton (1962) formula with hydrogen-like threshold cross-sections.

For Kr and all other species, level dissolution (pressure ionization) following Hummer & Mihalas (1988) and Hubeny et al. (1994) is accounted for. Stark broadening tables of Barnard et al. (1974) are used for He I $\lambda 4471\text{ Å}$ and of Schoening & Butler (1989) for He II lines.

4. Oscillator-strength calculations in krypton ions

New oscillator strengths were computed for transitions in Kr IV-VII ions in the present work. The method used was the same as the one considered in our previous studies that focused on Zn, Ga, Ge, Mo, and Ba ions (Rauch et al. 2014a, 2015b,

¹ <http://astro.uni-tuebingen.de/~TMAP>

² <http://astro.uni-tuebingen.de/~TMAD>

³ <http://www.g-vo.org>

⁴ <http://astro.uni-tuebingen.de/~TIRO>

⁵ <http://kurucz.harvard.edu/atoms.html>

2012, 2015a, 2014b), namely the Relativistic Hartree-Fock (HFR) method (Cowan 1981) that was modified to take core-polarization effects into account (HFR+CPOL), as described by Quinet et al. (1999, 2002). In each Kr ion, the same core-polarization parameters were used, i.e., a dipole polarizability $\alpha_d = 0.20 a_0^3$ and a cut-off radius $r_c = 0.55 a_0$. The former value, taken from Johnson et al. (1983), corresponds to a Kr^{8+} closed-shell ionic core of the type $1s^2 2s^2 2p^6 3s^2 3p^6 3d^{10}$, while the latter value was chosen as the mean value of $\langle r \rangle$ for the outermost core orbital (3d), as calculated by the HFR approach. Intravalence correlations were considered by explicitly including the following configurations in the physical models:

Kr IV $4s^2 4p^3 + 4s^2 4p^2 5p + 4s^2 4p^2 6p + 4s^2 4p^2 4f + 4s^2 4p^2 5f + 4s^2 4p^2 6f + 4s 4p^3 4d + 4s 4p^3 5d + 4s 4p^3 6d + 4s 4p^3 5s + 4s 4p^3 6s + 4s^2 4p 4d^2 + 4s^2 4p 4f^2 + 4p^5 + 4p^4 4f$ (odd parity) and $4s 4p^4 + 4s^2 4p^2 4d + 4s^2 4p^2 5d + 4s^2 4p^2 6d + 4s^2 4p^2 5s + 4s^2 4p^2 6s + 4s 4p^3 4f + 4s 4p^3 5f + 4s 4p^3 6f + 4s 4p^3 5p + 4s 4p^3 6p + 4p^4 4d + 4p^4 5s$ (even parity),

Kr V $4s^2 4p^2 + 4s^2 4p 5p + 4s^2 4p 6p + 4s^2 4p 4f + 4s^2 4p 5f + 4s^2 4p 6f + 4s 4p^2 4d + 4s 4p^2 5d + 4s 4p^2 6d + 4s 4p^2 5s + 4s 4p^2 6s + 4s^2 4d^2 + 4s^2 4f^2 + 4p^4 + 4p^3 4f$ (even parity) and $4s 4p^3 + 4s^2 4p 4d + 4s^2 4p 5d + 4s^2 4p 6d + 4s^2 4p 5s + 4s^2 4p 6s + 4s 4p^2 4f + 4s 4p^2 5f + 4s 4p^2 6f + 4s 4p^2 5p + 4s 4p^2 6p + 4p^3 4d + 4p^3 5s$ (odd parity),

Kr VI $4s^2 4p + 4s^2 5p + 4s^2 6p + 4s^2 4f + 4s^2 5f + 4s^2 6f + 4s 4p 4d + 4s 4p 5d + 4s 4p 6d + 4s 4p 5s + 4s 4p 6s + 4p^3 + 4p^2 4f + 4s 4d 4f + 4p 4d^2 + 4d^2 4f + 4p 4f^2$ (odd parity) and $4s 4p^2 + 4s^2 4d + 4s^2 5d + 4s^2 6d + 4s^2 5s + 4s^2 6s + 4s 4p 5p + 4s 4p 6p + 4s 4p 4f + 4s 4p 5f + 4s 4p 6f + 4p^2 4d + 4p^2 5s + 4s 4d 5s + 4s 4d^2 + 4s 4f^2$ (even parity),

Kr VII $4s^2 + 4p^2 + 4d^2 + 4f^2 + 5s^2 + 4s 4d + 4s 5d + 4s 6d + 4s 5s + 4s 6s + 4p 4f + 4p 5f + 4d 5s + 4p 5p$ (even parity) and $4s 4p + 4s 5p + 4s 6p + 4s 4f + 4s 5f + 4s 6f + 4p 5s + 4p 4d + 4p 5d + 4d 4f$ (odd parity).

The HFR+CPOL method was then combined with a semi-empirical optimization of the radial parameters to minimize the discrepancies between calculated and experimental energy levels. More precisely, the energy levels reported by Saloman (2007) were used in Kr IV to adjust the radial parameters corresponding to the $4p^3$, $4p^2 5p$, $4s 4p^4$, $4p^2 4d$, $4p^2 5d$, $4p^2 5s$, and $4p^2 6s$ configurations. In Kr V, the experimental level values taken from Saloman (2007) and Rezende et al. (2010) were included in the adjustment of some parameters in the $4p^2$, $4p 5p$, $4s 4p^2 4d$, $4p^4$, $4s 4p^3$, $4p 4d$, $4p 5d$, $4p 5s$, and $4p 6s$ configurations. In the case of Kr VI, the energy levels from Saloman (2007) and Farias et al. (2011) enabled us to optimize the radial parameters by describing the $4p$, $5p$, $4s 4p 4d$, $4p^3$, $4s 4p^2$, $4s^2 4d$, $4s^2 5s$, $4s 4p 4f$, $4s 4p 5p$, and $4p^2 4d$ configurations. Finally, the energy levels measured by Raineri et al. (2014) were used to fit the parameters of the $4s^2$, $4p^2$, $4s 4d$, $4s 5d$, $4s 6d$, $4s 5s$, $4s 6s$, $4p 4f$, $4s 4p$, $4s 5p$, $4s 6p$, $4s 4f$, $4s 5f$, $4s 6f$, $4p 5s$, and $4p 4d$ configurations in Kr VII.

The numerical values of the parameters adopted in the present calculations are reported in Tables 2-5, while the computed energies for Kr IV-VII are compared with available experimental values in Tables 6-9, respectively. Tables 10-13 give the computed oscillator strengths ($\log gf$) and transition probabilities (gA , in s^{-1}) for Kr IV-VII, respectively, and the numerical values (in cm^{-1}) of lower and upper energy levels, together with the corresponding wavelengths (in \AA). The cancellation factor, CF, as defined by Cowan (1981) is also given in the last column of each table. For a specific transition, a very small value of this parameter (typically < 0.05) indicates strong cancellation effects in the calculation of the line strength. In this case, the corre-

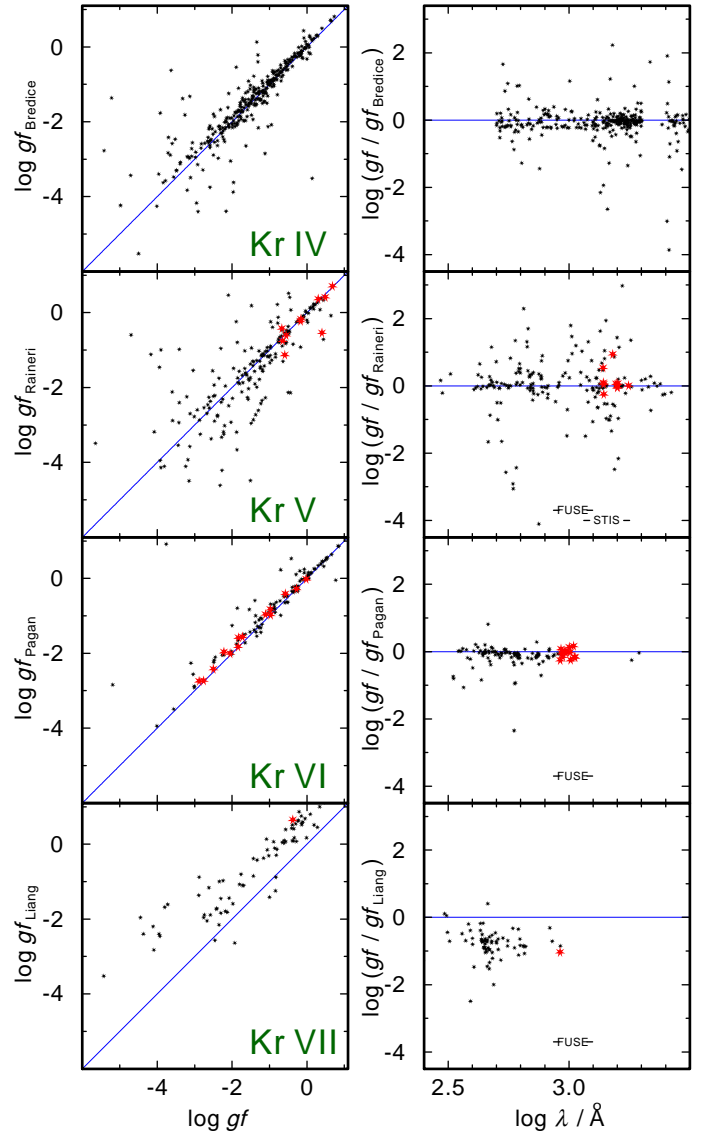


Fig. 1. Comparison of our weighted oscillator strengths for Kr IV-VII (from top to bottom) to those of Bredice et al. (2000), Raineri et al. (2012), Pagan et al. (1996), and Liang et al. (2013), respectively. Left panel: Comparison of weighted oscillator strengths. Right panel: Ratio of weighted oscillator strengths over wavelength. The wavelength ranges of our FUSE and HST/STIS spectra are marked. The larger, red symbols refer to the lines identified in RE 0503–289 (see Figs. 5 and 8).

sponding oscillator strength and transition probability could be affected by larger uncertainties and, as a consequence, should be considered with care.

Tables 10-13 are provided in VO⁶-compliant format via the registered⁷ Tübingen Oscillator Strengths Service (TOSS⁸, Rauch et al. 2015a) that has recently been developed by GAVO.

For Kr IV-VII, oscillator strengths were previously published by several authors. In the following, we compare our new data to theirs. Figure 1 illustrates this comparison.

Bredice et al. (2000) calculated weighted oscillator strengths for 471 spectral lines of Kr IV involving the $4s^2 4p^3$, $4s 4p^4$, $4s^2 4p^2 5p$, and $4s^2 4p^2 (5s + 6s + 4d + 5d)$ configurations within the wavelength interval $[501.50 \text{ \AA}, 4703.85 \text{ \AA}]$. Of these lines,

⁶ Virtual Observatory

⁷ cf., <http://dc.zah.uni-heidelberg.de/wirr/q/ui/fixed>

⁸ <http://dc.g-vo.org/TOSS>

320 agree within 0.1 Å to lines reported in Table 10. We selected them to compare their $\log gf$ values to ours in Fig. 1. As seen from this figure, even if both sets of results agree for many lines, a large scatter is also observed for many other lines. This is obviously due to the very limited multiconfiguration Hartree-Fock model (including only two odd- and seven even-parity configurations) that were considered by Bredice et al. (2000).

Raineri et al. (2012) published transition probabilities for 313 lines of Kr v ([294.27 Å, 3614.10 Å]). They were calculated with Cowan's package (Cowan 1981), i.e., the Hartree-Fock method with relativistic corrections using energy parameters from least-squares and dipole-reduced matrix from a core polarization calculation. A large set of $4s^24p^2$, $4p5p$, $4p^4$, $4s4p^24d$, $4p4f$, $4s4p^25s$, $4s^24d^2$, $4s4p4d5p$, $4p^34f$, $4s4p4d4f$, $4s^24f^2$, and $4s4d^3$ even and $4s4p^3$, $4p4d$, $4p5s$, $4p5d$, $4p6s$, $4p5g$, $4p6d$, $4s4p^25p$, $4s4p^24f$, $4p^34d$, $4s4p^26p$, $4s4p4d^2$, $4p^35s$, $4s^24d4f$, $4s^24f5s$, $4p^35d$, $4s^24f5d$, $4s4d^25p$, and $4s4d^24f$ odd configurations was considered.

We selected 183 of these lines (by wavelength agreement within 0.1 \AA to lines in Table 11) and compared their $\log gf$ values to ours (Fig.1). Although a good agreement between the two sets of data is observed for many lines, a large scatter is also obtained for a number of transitions, in particular for those corresponding to weak oscillator strengths, i.e., $\log gf < -2$. This is mainly due to the rather large cancellation effects that appear in the calculations of these types of transition rates in both works. Moreover, it is worth noting that Raineri et al. (2012) modified only their electric dipole matrix elements to take core-polarization effects into account while, in our work, all the radial wave functions were also modified by a model potential, including one- and two-body core-polarization contributions, together with a core-penetration correction (see, e.g., Quinet et al. 2002). This could also explain some of the differences between the two sets of results.

Pagan et al. (1996) calculated 138 weighted Kr vi oscillator strength ($[331.65 \text{ \AA}, 2051.72 \text{ \AA}]$) in a multiconfigurational HFR approach considering $4s^2 4p$, $4p^3$, $4s^2 5p$, $4s 4p 4d$, $4s^2 4f$, $4s 4p 5s$, $4s^2 6p$, $4s 4d 4f$, $4p^2 4f$, $4p 4d^2$, and $4d^2 4f$ configurations for odd parity and $4s 4p^2$, $4s^2 4d$, $4s^2 5s$, $4s^2 5d$, $4s 4p 4f$, $4s 4p 5s$, $4p^2 4d$, and $4s 4d^2$ for even parity. Analogously to Kr v, we compared the $\log gf$ values of 115 selected Kr vi lines with our data (Fig.1). Although both sets of data are in good agreement, we note that our oscillator strengths are generally smaller than those obtained by Pagan et al. (1996). This is essentially due to the much more extended multiconfiguration expansions and the core-polarization effects that we include in our calculations.

Liang et al. (2013) presented oscillator strengths for 90 lines ([201.05 Å, 920.98 Å]) For Kr VII. For their calculations with the AUTOSTRUCTURE code (Badnell 2011), they only use nine configurations, i.e., $4s^2$, $4p^2$, $4s4d$, $4s5s$, $4s5d$, and $4s4p$, $4s4f$, $4p4d$, $4s5p$ for the even and odd parities, respectively. In particular, they omit some configurations, such as $4d^2$ and $4d4f$ which, according to our calculations, appeared to have non-negligible interactions with $4s^2$, $4p^2$ and $4s4p$, $4s4f$, $4p4d$, respectively. The effect of this rather limited model is illustrated in Fig.1, where our $\log gf$ values, obtained with an extended configuration interaction approach, are systematically smaller than those reported by Liang et al. (2013).

5. Effective temperature and surface gravity

Dreizler & Werner (1996) analyzed the optical TWIN spectra (Sect. 2) with NLTE model atmospheres that consid-

Table 14. Photospheric abundances of RE 0503–289. IG is a generic model atom (Rauch & Deetjen 2003) comprising Ca, Sc, Ti, V, Cr, Mn, and Co. [X] denotes \log (fraction/solar fraction) of species X.

Element	Mass fraction	
	Our models	Werner et al. (2012b)
He	9.73×10^{-1}	9.78×10^{-1}
C	2.22×10^{-2}	2.00×10^{-2}
N	5.49×10^{-5}	5.50×10^{-5}
O	2.94×10^{-3}	2.00×10^{-3}
Si	1.60×10^{-4}	
P	1.06×10^{-6}	
S	3.96×10^{-5}	
IG	9.98×10^{-7}	
Fe	1.30×10^{-5}	
Ni	7.25×10^{-5}	
Zn	1.13×10^{-4}	
Ga	3.44×10^{-5}	
Ge	1.58×10^{-4}	
As	1.60×10^{-5}	
Kr	5.04×10^{-4}	6.00×10^{-5}
Mo	1.88×10^{-4}	
Sn	2.04×10^{-4}	
Xe	6.29×10^{-5}	6.00×10^{-5}
Ba	3.57×10^{-4}	

ered opacities of H, He, C, N, O, and Si. They derived $T_{\text{eff}} = 70\,000 \pm 5000$ K and $\log(g/\text{cm/s}^2) = 7.5 \pm 0.3$. In their spectral analysis based on H+He composed LTE model atmospheres, Vennes et al. (1998) determined $T_{\text{eff}} = 68\,600 \pm 1800$ K and $\log g = 7.20 \pm 0.07$. Dreizler (1999) improved the metal abundance analysis of C, N, O, and Ni based on HST/GHRS (Goddard High-Resolution Spectrograph) observations and used the previously determined $T_{\text{eff}} = 70\,000$ K and $\log g = 7.5$. The same did Werner et al. (2012b) for their Kr and Xe abundance analysis. In our latest models, much more species (Table 14) and, thus, a higher metal opacity is considered. Therefore, we start here with a new assessment of T_{eff} and $\log g$.

The decrements of spectral series are very sensitive indicators for $\log g$ (e.g., Rauch et al. 1998; Ziegler et al. 2012). Figure 2 shows a comparison of theoretical line profiles of the He II Fowler series (principal quantum numbers $n - n'$ with $n = 3$ and $n' \geq 4$) that are located in our HST/STIS spectrum. The central depressions of He II 3 – [5, . . . , 13] are well matched at $\log g = 7.5$, while the decrement is much too strong at $\log g = 8.0$, and much too weak at $\log g = 7.0$. We therefore verify $\log g = 7.5$, which was the result of Dreizler & Werner (1996), and improved the error limit to ± 0.1 dex.

Figure 4 demonstrates that the line wings of the He II $n = 2$ and $n' \geq 3$ $n = 4$ and $n' \geq 5$ (Pickering) series are well in agreement with the observation at $\log g = 7.5$. A different $\log g$ cannot be compensated for by adapted interstellar H I densities because this has a strong impact on the inner line wings (Sect. 6). The error range for these densities is below 20%. Our optical spectra corroborate the $\log g$ determination. Figure 4 shows the comparison of our models to the observations. He II $\lambda 6560 \text{ \AA}$ is too shallow in all our models and does not match the TWIN observation. The reason is still unknown. The UVES spectra show a slightly better fit of this line, which may be a hint for some data-reduction uncertainty in the TWIN and/or UVES spectra. To make a comparison with the FUSE observation, we selected

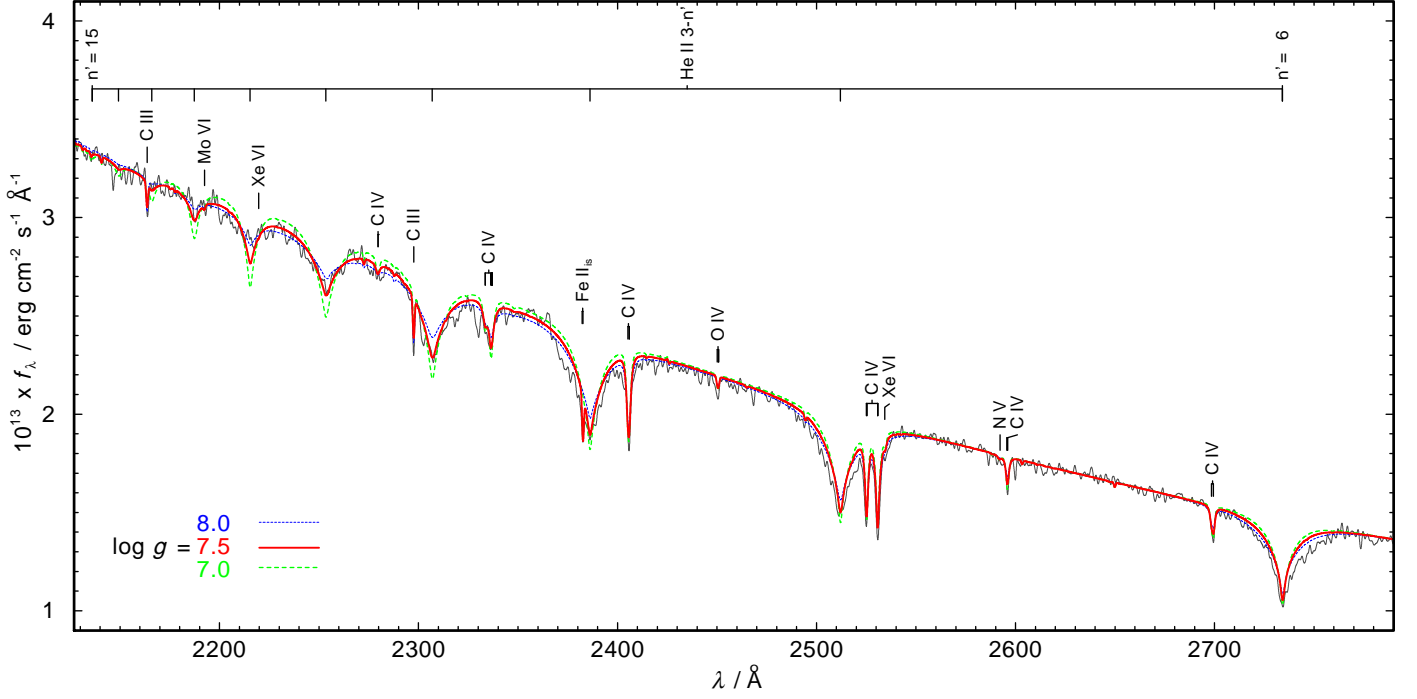


Fig. 2. Section of the HST/STIS spectrum, compared with models with different $\log g$ of 7.0 (thin, green, dashed), 7.5 (thick, red), and 8.0 (thin, blue, dashed) and $T_{\text{eff}} = 70\,000\text{ K}$. The synthetic spectra are normalized to match the flux of the models at 2800 \AA , respectively. All spectra are convolved with Gaussians (full width at half maximum of 1 \AA) for clarity. Identified lines are indicated. “is” denotes interstellar origin.

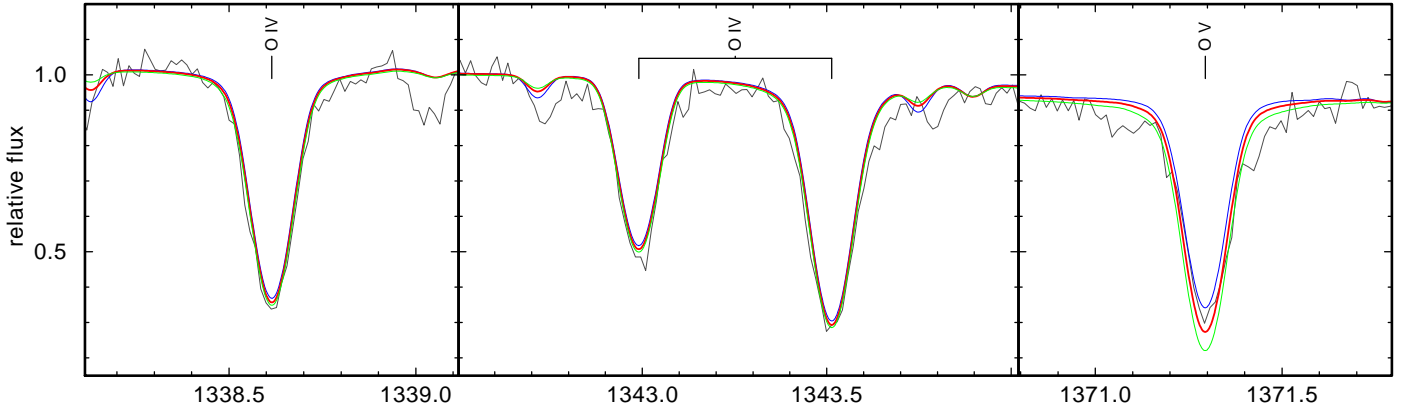


Fig. 3. Sections of the HST/STIS spectrum compared with three $\log g = 7.5$ models with different T_{eff} of $66\,000\text{ K}$ (thin, blue), $70\,000\text{ K}$ (thick, red), and $74\,000\text{ K}$ (thin, green). The synthetic spectra are normalized to match the observed flux at 1335 \AA .

those $\text{He II } n = 2 - n'$ lines that are not contaminated by interstellar H I line absorption. Their observed line profiles and the series' decrement are well reproduced at $\log g = 7.5$. The insufficient blaze correction of the HST/STIS spectrum only allows for an evaluation of the inner line wings of $\text{He II } \lambda 1640.42\text{ \AA}$ ($n = 2 - 3$). $\text{He II } \lambda 1215.12\text{ \AA}$ ($n = 2 - 4$) is shown in Fig. 13.

Dreizler & Werner (1996) used the O IV/O V ionization equilibrium as an indicator for T_{eff} . They found a simultaneous match of theoretical line profiles of $\text{O IV } \lambda\lambda 1338.6, 1343.0, 1343.5\text{ \AA}$ ($2p^2\text{ }^2\text{P} - 2p^3\text{ }^2\text{D}^0$) and $\text{O V } \lambda 1371.3\text{ \AA}$ ($2p\text{ }^1\text{P}^0 - 2p^2\text{ }^1\text{D}$) to a high-resolution IUE observation. In Fig. 3, we show the same lines compared to our much better HST/STIS observation. $\text{O V } \lambda 1371.3\text{ \AA}$ appears much more sensitive to T_{eff} , compared to the O IV lines, and $T_{\text{eff}} = 70\,000\text{ K}$ is verified within an error range of 2000 K .

We adopt $T_{\text{eff}} = 70\,000 \pm 2000\text{ K}$ and $\log g = 7.5 \pm 0.1$. Many additional ionization equilibria, e.g., of He I - II (Fig. 4), C III

- IV (Fig. 2), O IV - V (Dreizler & Werner 1996, and this paper, Fig. 3), Zn IV - V (Rauch et al. 2014a), Ga IV - V (Rauch et al. 2015b), Ge IV - V (Rauch et al. 2012), Kr V - VII (Werner et al. 2012b, and this paper), Mo V - VI (Rauch et al. 2015a), Xe VI - VII (Werner et al. 2012b), and Ba VI - VII (Rauch et al. 2014b) are well matched at these values.

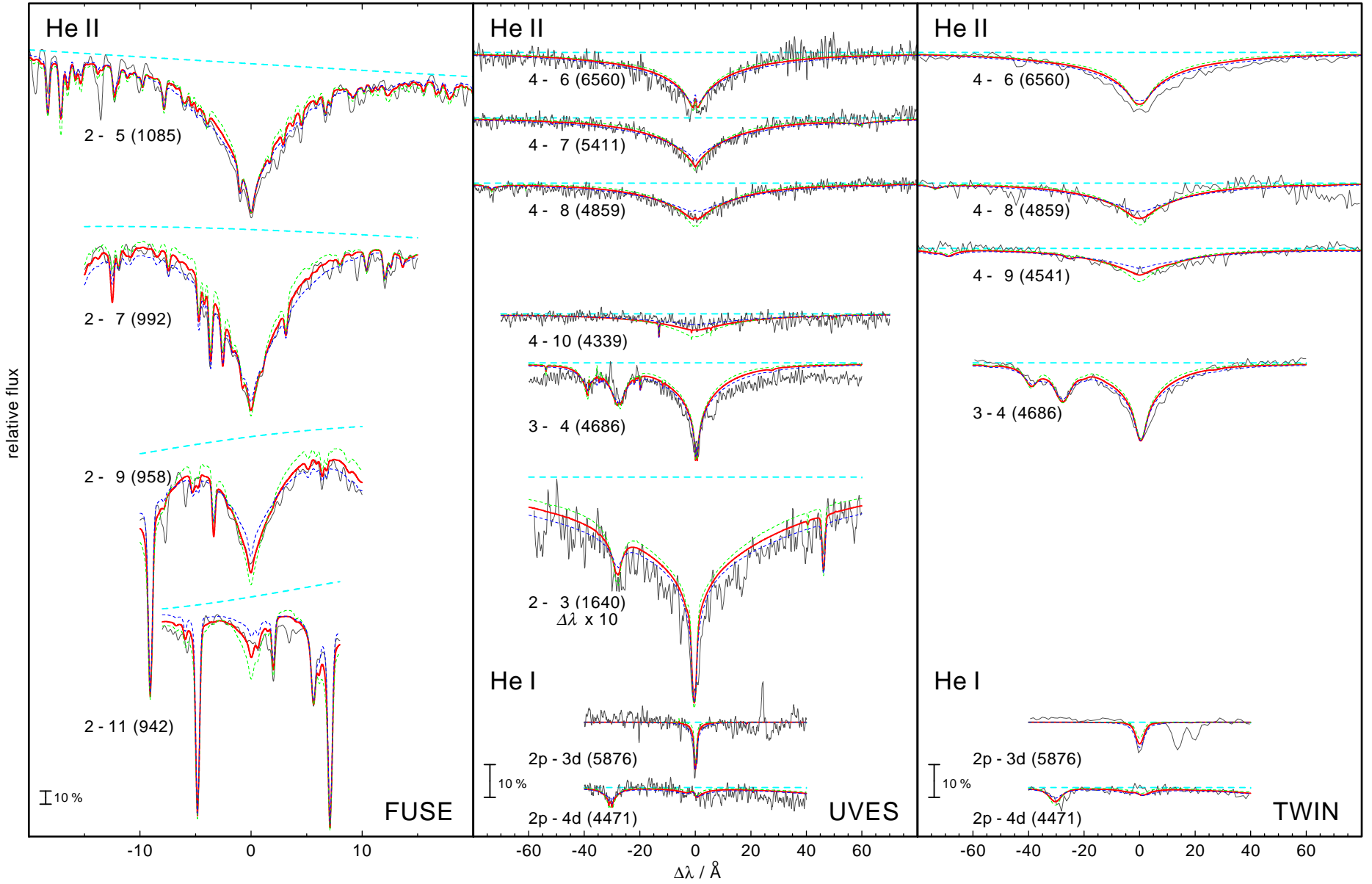


Fig. 4. Three models ($T_{\text{eff}} = 70\,000\text{ K}$) with $\log g = 7.0$ (green, dashed), 7.5 (red), and 8.0 (blue, dashed) compared to FUSE (left panel), UVES (middle), and TWIN (right) observations. The dashed, horizontal lines indicate the location of the local continuum.

6. Line identification and abundance analysis

We replaced our previously used Kr model atom and recalculated our latest model atmosphere (see Rauch et al. 2015a). Figure 5 shows that, in general, the wavelengths of the old and the new data are in good agreement, while the line strengths calculated with the new data are much smaller. There are three reasons for this deviation. First, the Kr IV–VII model ions are much more complete, e.g., for Kr VI and Kr VII, Werner et al. (2012b) constructed model ions with 46 and 14 atomic levels that were combined with 140 and 2 line transitions with known oscillator strengths, respectively. These numbers were increased to 69 and 70 levels with 843 and 743 line transitions, respectively (Table 1). Second, the new oscillator strengths of the lines that were used in the Kr abundance analysis are smaller in general (Table 15). Third (with minor impact), the chemical composition of the model atmospheres is different and the C, N, and O abundances were fine-tuned, i.e., the background opacity was increased and, thus, the calculated atmospheric structure is different.

In their Kr abundance analysis, Werner et al. (2012b) use He+C+N+O+Kr+Xe models and adopt the C, N, and O abundances of Dreizler (1999). Our models also consider the opacities of Si, P, S, Ca, Sc, Ti, V, Cr, Mn, Fe, Co, Ni, Zn, Ga, Ge, As, Mo, Sn, and Ba. The C and O abundances were increased to better reproduce their observed lines. The abundances are compared in Table 14. Figure 6 shows the temperature structures of the respective models. Deviations are obvious in the outer atmosphere, but also in the line-forming region ($-4 \leq \log m \leq +0.5$, m is the column mass, measured from the outer boundary of our model atmospheres).

Due to the higher background opacity in our models, the calculated Kr lines are weaker compared with Werner et al. (2012b, $\log \text{Kr} = -4.3 \pm 0.5$). To match the observation, we have to increase the previously determined Kr mass fraction ($\log \text{Kr} = -4.3 \pm 0.5$, Werner et al. 2012b) by a factor of 10 to 5.1×10^{-4} ($\log \text{Kr} = -3.3 \pm 0.3$). Our given error is estimated, considering the error propagation that is due to the uncertainties of T_{eff} , $\log g$ and the background opacity (Sect. 5).

Figure 7 shows that Kr V–VII are the dominant ions in the line-forming region. We newly identified Kr VI λ 1052.067 Å ($\log gf = -0.55$) in the FUSE observation and for the first time lines of Kr V, namely $\lambda\lambda$ 1384.611, 1387.961, 1392.594, 1393.603, 1515.611, 1566.073, 1583.456, 1589.269, 1591.875, 1764.478 Å ($-0.59, -0.65, -0.67, -0.17, 0.40, 0.30, 0.25, 0.68, 0.49, -0.16$, respectively) in the HST/STIS observation (Fig. 8). These lines are in agreement with the observation, while Kr V $\lambda\lambda$ 1583.456, 1591.875, 1764.478 Å are uncertain. Many more weak Kr V–VII lines are exhibited in the synthetic spectrum but they fade in the noise of the available observed UV and optical spectra. The Kr V–VII ionization equilibrium is well matched. Since ionization equilibria are sensitive indicators of the effective temperature, our value of $T_{\text{eff}} = 70\,000$ K (Sect. 5) is corroborated.

With our new Kr oscillator strengths and also at the higher Kr abundance, a simultaneous fit of all 26 identified lines was achieved. For example, Kr VI $\lambda\lambda$ 944.046, 965.093, 1011.133, 1015.765, 1052.964 Å were much too weak before in our models but now reproduce the observation (Fig. 5).

In the optical wavelength range, Kr V λ 3579.739 Å ($\log gf = -1.15$, air wavelength 3578.717 Å) is the strongest line in our model but very weak (central depression of about 1 % of the local continuum flux) and not detectable in the available observation.

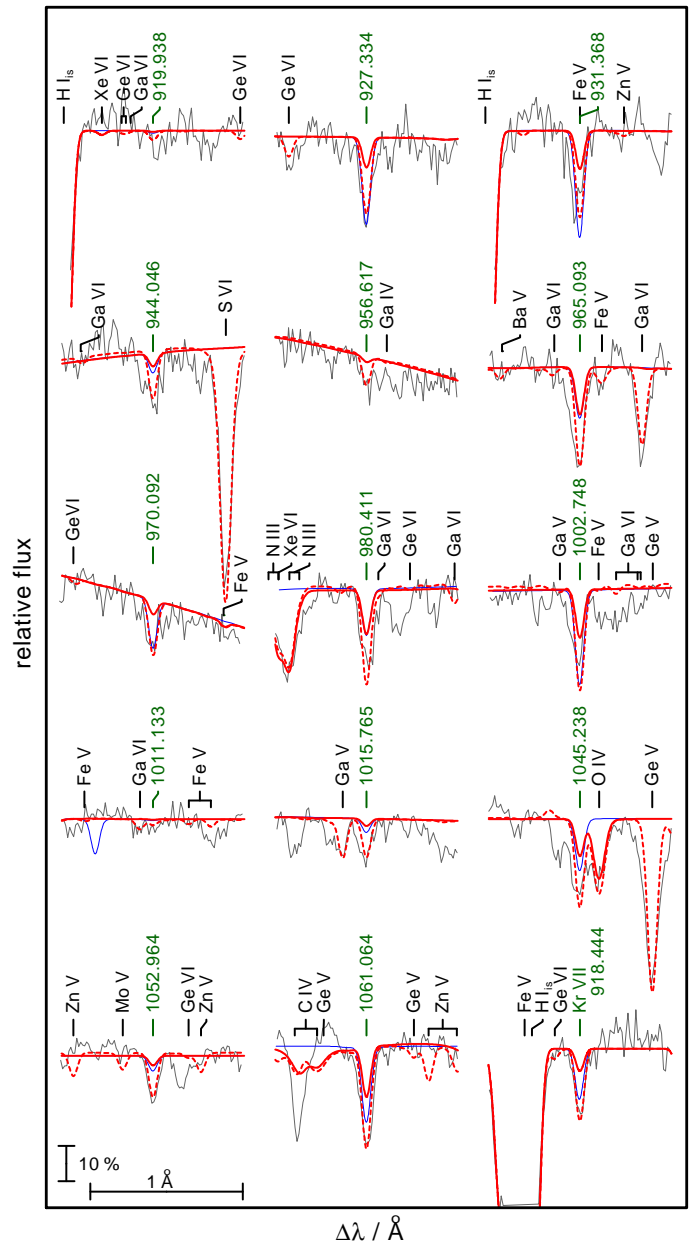


Fig. 5. Kr VI lines and one Kr VII line (bottom right) identified by Werner et al. (2012b) in the observed FUSE spectrum of RE 0503–289. Three synthetic spectra are overplotted. Thin, blue: the genuine spectrum of Werner et al. (2012b, $T_{\text{eff}} = 70\,000$ K), classical Kr model atom with $\log \text{Kr} = -4.3$. Thick red ($T_{\text{eff}} = 70\,000$ K): our new Kr model atom with $\log \text{Kr} = -4.3$. Dashed, red ($T_{\text{eff}} = 70\,000$ K): our new Kr model atom with $\log \text{Kr} = -3.3$. Kr lines are indicated with their wavelengths from Tables 12 and 13, and other lines by their ion’s name. “is” denotes interstellar origin.

Ba VII lines were newly identified in the observed FUSE spectrum during the search for Kr lines. These are one blend at Ba VII $\lambda\lambda$ 924.892, 924.898 Å ($\log gf = -2.42$ and -2.06 , respectively, Fig. 12), and Ba VII λ 1143.317 Å (-2.54). Rauch et al. (2014b) previously discovered Ba VII λ 943.102 Å (-1.77) and Ba VII λ 993.411 Å (-1.57).

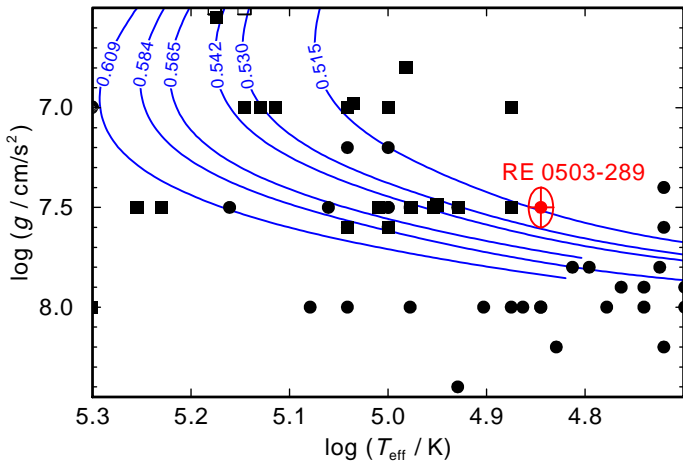


Fig. 9. Location of RE 0503–289 in the $\log T_{\text{eff}} - \log g$ diagram (the ellipse indicates the error range) compared with evolutionary tracks for post-AGB stars that experienced a very late thermal pulse (Althaus et al. 2009). These are labeled with the respective stellar masses (in M_{\odot}). Positions of hydrogen-deficient PG 1159-type stars and DO-type WDs are indicated by squares and circles, respectively.

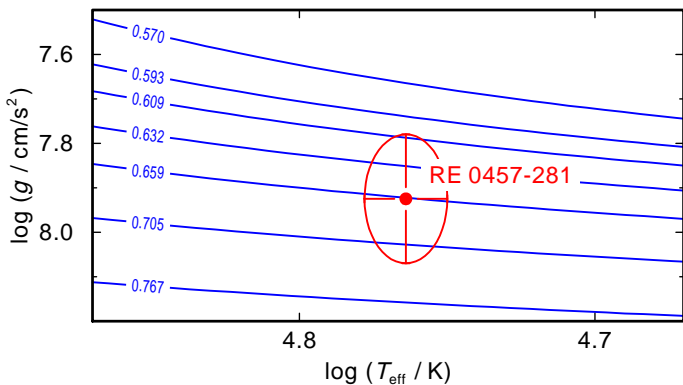


Fig. 10. Location of RE 0457–281 ($T_{\text{eff}} = 55\,875 - 60\,170$ K, $\log g = 7.78 - 8.07$, Marsh et al. 1997, the ellipse indicates the error range) in the $\log T_{\text{eff}} - \log g$ diagram compared with evolutionary tracks for DA-type WDs (Renedo et al. 2010) labeled with the respective stellar masses (in M_{\odot}).

We used the flux calibration⁹ of Heber et al. (1984) to calculate the distance

$$d = 7.11 \times 10^4 \times \sqrt{H_{\nu} M \times 10^{0.4 m_{\nu_0} - \log g}} \text{ pc},$$

using $m_{\nu_0} = m_{\nu} - R_{\nu} E_{B-V}$, and the Eddington flux $H_{\nu} = 1.018 \pm 0.002 \times 10^{-3} \text{ erg/cm}^2/\text{s/Hz}$ at $\lambda_{\text{eff}} = 5454 \text{ \AA}$ of our final model atmosphere. We used $E_{B-V} = 0.015 \pm 0.002$, $M = 0.514^{+0.015}_{-0.005} M_{\odot}$, and $m_{\nu} = 13.58 \pm 0.01$ (Faedi et al. 2011). We derive $d = 147^{+16}_{-18} \text{ pc}$. The height below the Galactic plane¹⁰ is $z = 84^{+9}_{-10} \text{ pc}$. This distance is smaller than the value of Vennes et al. (1998, 190 pc).

8. Interstellar line absorption

To measure the interstellar reddening in the line of sight (LOS), we first normalized our synthetic spectrum ($T_{\text{eff}} = 70\,000 \text{ K}$,

⁹ <http://astro.uni-tuebingen.de/~rauch/SpectroscopicDistanceDetermination.pdf>

¹⁰ Galactic coordinates of RE 0503–289 for J2000: $l = 230:6717$, $b = -34:9355$

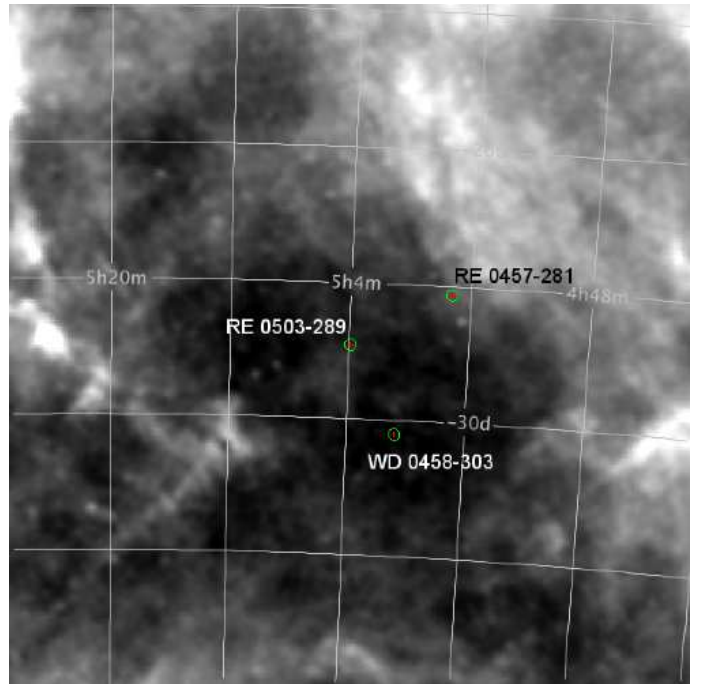


Fig. 11. Locations (J2000) of RE 0503–289, RE 0457–281, and WD 0458–303 (marked by green encircled red + signs) in a $10^{\circ} \times 10^{\circ}$ 100μ dust map from <http://irsa.ipac.caltech.edu/applications/DUST>.

$\log g = 7.5$) to match the measured $m_{\text{H}} = 14.77$ (Cutri et al. 2003). Then, interstellar reddening with $E_{B-V} = 0.015 \pm 0.002$ had to be applied to reproduce the observed FUV continuum flux, using the reddening law of Fitzpatrick (1999) with the standard $R_{\nu} = 3.1$. Our E_{B-V} value is in good agreement with measurements of Schlegel et al. (1998, evaluating images from the Diffuse Infrared Background Experiment on board of the Cosmic Background Explorer satellite, COBE/DIRBE, and the Infrared Astronomy Satellite Sky Survey Atlas, IRAS/ISSA) and Schlafly & Finkbeiner (2011, based on Sloan Digital Sky Survey, SDSS, stellar spectra). They publish $E_{B-V} = 0.0160$ and $E_{B-V} = 0.0138$, respectively. The errors can be estimated from the mean values of E_{B-V} within a 5° circle around RE 0503–289. These are $E_{B-V}^{\circ} = 0.0155 \pm 0.0008$ and 0.0134 ± 0.0006 , respectively. The dust distribution around RE 0503–289 and RE 0457–281 is illustrated by Fig. 11. While RE 0503–289 is apparently located in the middle of a voided area, RE 0457–281 lies at the rim of stronger emission, with a higher $E_{B-V} = 0.0201$ ($E_{B-V}^{\circ} = 0.0203 \pm 0.0004$, Schlafly & Finkbeiner 2011).

The DAO-type WD 0458–303 (MCT 0458–3020, $m_{\text{B}} = 16.3$, $T_{\text{eff}} = 91\,010 \pm 3156 \text{ K}$, $\log g = 7.09 \pm 0.10$, $M = 0.53 \pm 0.02 M_{\odot}$, $d = 928 \text{ pc}$, Demers et al. 1986; McCook & Sion 1999a,b; Gianninas et al. 2010, 2011) also lies close to RE 0503–289 (angular distance $1^{\circ}53$, Fig. 11) in an area with obviously less 100μ emission and a lower $E_{B-V} = 0.0082$ ($E_{B-V}^{\circ} = 0.0085 \pm 0.0005$, Schlafly & Finkbeiner 2011).

While RE 0503–289 and RE 0457–281 were newly identified in the ROSAT/WFC (Röntgensatellit/Wide Field Camera) extreme-ultraviolet (EUV) bright source catalogue (Pounds et al. 1993; Pounds & et al. 1993) and were later matched with their optical counterparts (Mason et al. 1995, 1996), the much hotter WD 0458–303 has no significant EUV flux. Therefore, an investigation, based on UV spectroscopy, of the ISM line absorption in the LOS toward this much more distant star is highly

desirable. So far, only Galaxy Evolution Explorer (GALEX¹¹) near and far UV imaging is available in MAST. Exploiting the GALEX GR6 and GR7 data releases, GalexView¹² provides $m_{\text{FUV}} = 14.35 \pm 0.01$, $m_{\text{NUV}} = 15.08 \pm 0.01$ and $E_{\text{B-V}} = 0.0096$ for WD 0458–303.

Figure 12 shows a section of the FUSE observation compared with our spectrum that was calculated with the new Kr model atom and $\log \text{Kr} = -3.3$. $\text{Kr VII } \lambda 918.444 \text{ \AA}$ and $\text{Kr VI } \lambda \lambda 927.334, 931.368 \text{ \AA}$ are prominent in the observed spectrum and are well reproduced, while $\text{Kr V } \lambda 916.734 \text{ \AA}$ and $\text{Kr VI } \lambda 919.938 \text{ \AA}$ are weak in our model and fade in the noise of the observation.

The program *OWENS* was used to model the line absorption by the interstellar medium (ISM). *OWENS* is able to consider individual ISM clouds with different radial and turbulent velocities, temperatures, column densities, and chemical compositions. Voigt profiles are fitted to the observation using a χ^2 minimization. More details are given by, for example, Hébrard et al. (2002) or Hébrard & Moos (2003). To model the interstellar absorption of neutral hydrogen, we first considered two clouds with column densities of $N_{\text{H I}} = 1.2 \times 10^{18} \text{ cm}^{-2}$ and $N_{\text{H I}} = 9.3 \times 10^{15} \text{ cm}^{-2}$, and radial velocities of $v_{\text{rad}}^{\text{ISM}} = +10.0$ and -39.3 km s^{-1} , respectively. These column densities are smaller than the expected value of $9.2 \pm 0.3 \times 10^{18} \text{ cm}^{-2}$ that was calculated from $N_{\text{H}} / E_{\text{B-V}} = 6.12 \pm 0.20 \times 10^{21} \text{ atoms cm}^{-2} \text{ mag}^{-1}$ (Gudennavar et al. 2012, with $N_{\text{H}} = N_{\text{H I}} + 2N(\text{H}_2)$). In addition, we derive $v_{\text{rad}}^{\text{RE 0503-289}} - v_{\text{rad}}^{\text{ISM}} = 14.5 \pm 4.2 \text{ km s}^{-1}$ and $64.8 \pm 4.2 \text{ km s}^{-1}$ for the two clouds.

Vennes et al. (1994) analyzed Extreme Ultraviolet Explorer (EUVE) photometry data and measured column densities of $\log(N_{\text{H I}} / \text{cm}^{-2}) = 17.75\text{--}18.00$ and $17.80\text{--}17.90$ in the LOS toward RE 0503–289 and the nearby (spatially separated by $1^\circ 66'$) RE 0457–281. Since Hoare et al. (1993) and Vallerga et al. (1993) determined $\log(N_{\text{H I}} / \text{cm}^{-2}) = 18.00\text{--}18.18$ for β and ϵ CMa (located in about the same direction, at angular distances of 21° and 31° , respectively, but at larger distances of $d = 206 \text{ pc}$ and $d = 188 \text{ pc}$, respectively), Vennes et al. (1994) suggested that the local cloud, agglomerated with a few parsecs from the Sun, is the main ISM structure along the LOS toward these stars. Vennes et al. (1998) used ORFEUS/BEFS¹³ observations and measured $v_{\text{rad}}^{\text{RE 0503-289}} - v_{\text{rad}}^{\text{ISM}} = 48 \pm 21 \text{ km s}^{-1}$, which is within error limits in agreement with the mean velocity of our two clouds. Dupuis et al. (1995) investigated interstellar column densities based on EUVE spectra. For RE 0457–281, they found $d = 90 \text{ pc}$ and $\log(N_{\text{H I}} / \text{cm}^{-2}) = 18.04\text{--}18.12$.) measured $v_{\text{rad}}^{\text{RE 0457-281}} = 80 \pm 12 \text{ km s}^{-1}$. Pauli et al. (2006) investigated on the 3D kinematics of WDs from the SPY project and determined $v_{\text{rad}}^{\text{RE 0457-281}} = 49.2 \pm 11.5 \text{ km s}^{-1}$ and a distance of $d = 115.9 \pm 14 \text{ pc}$.

The interstellar $\text{N II } \lambda 915.6 \text{ \AA}$ also exhibits a double feature (Fig. 12). We considered this line with column densities of $N_{\text{N II}} = 7.5 \times 10^{13} \text{ cm}^{-2}$ at $+11.0 \text{ km s}^{-1}$ and $N_{\text{N II}} = 2.5 \times 10^{13} \text{ cm}^{-2}$ at -39.5 km s^{-1} . The HST/STIS observation is used to verify our solution with two ISM clouds (Fig. 13). While $\text{Si III } \lambda 1206.5 \text{ \AA}$ is not sufficiently well reproduced with $N_{\text{Si III}} = 1.8 \times 10^{13} \text{ cm}^{-2}$ at $+18.0 \text{ km s}^{-1}$ and $N_{\text{Si III}} = 1.9 \times 10^{12} \text{ cm}^{-2}$ at -40.5 km s^{-1} (insert A), a multi-cloud solution for the ISM absorption could improve

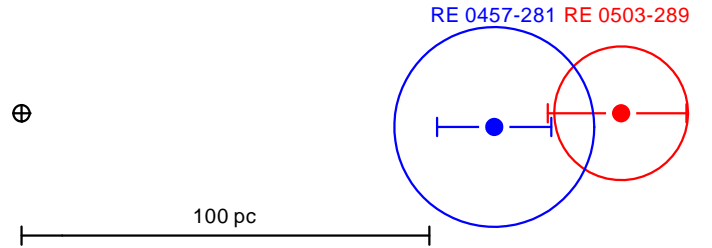


Fig. 15. Constellation of Earth, RE 0457–281, and RE 0503–289. The circles indicate the estimated maximum distance reached by stellar material that was ejected from the stars on the AGB.

the agreement (main spectra). The assumed clouds' column densities and radial velocities are summarized in Table 16.

While the outer line wings of $\text{H I } L\alpha$ are dominated by stellar He II absorption, the inner line wings are well matched at a total $N_{\text{H I}} = 1.5 \times 10^{18} \text{ cm}^{-2}$. To reproduce the blue side of the observed absorption core, a significant D I column density of $N_{\text{D I}} = 1.2 \times 10^{14} \text{ cm}^{-2}$ is necessary. This value is uncertain because this line is saturated and blended by stellar He II and interstellar H I . Therefore, we consider D I with a single ISM cloud at 12.1 km s^{-1} . The region around $L\alpha$ is well reproduced with either a two-cloud (insert “B”) or a multi-cloud solution for H I .

Figure 14 shows that a multi-cloud solution can explain the strong and weak ISM absorption lines in the observations of RE 0503–289 and RE 0457–281. To simulate the stellar flux of RE 0457–281, we used a synthetic spectrum (pure hydrogen, $T_{\text{eff}} = 58\,000 \text{ K}$, $\log g = 7.9$) which was provided by the German Astrophysical Virtual Observatory (GAVO¹⁴) Theoretical Stellar Spectra Access service (TheoSSA¹⁵). The ISM line absorption was modeled with the same parameters that were used for RE 0503–289. We find a good agreement for RE 0457–281 and RE 0503–289, although they have different distances of $116 \pm 14 \text{ pc}$ and $150^{+17}_{-18} \text{ pc}$, respectively, which are in rough agreement within their error limits (Fig. 15). This issue will be clarified by the results of GAIA¹⁶ in the near future.

This corroborates the suggestion of Vennes et al. (1994) that the major contribution to the ISM absorption stems from the so-called local fluff in which our Sun is located. Nearly all of the gas along the LOS toward RE 0503–289 and RE 0457–281, and at distances well beyond these, is very hot and highly ionized. The gas that we see occupies only a small fraction of the total distance to the stars.

The main interstellar gas component toward RE 0503–289 is located near $v_{\text{helio}} = +15 \text{ km s}^{-1}$, as evident from the $\text{H I } 21 \text{ cm}$ emission spectrum in this direction from the Leiden-Argentina-Bonn (LAB) survey (Kalberla et al. 2005). Also the STIS spectrum of RE 0503–289 indicates strong interstellar absorption at $v_{\text{helio}} \approx +15 \text{ km s}^{-1}$ in the strong resonance lines of $\text{C II } \lambda 1334.5 \text{ \AA}$, $\text{Si III } \lambda 1206.5 \text{ \AA}$, $\text{Si II } \lambda 1260.4 \text{ \AA}$, and others. As well as this main absorption component, there is weaker interstellar/circumstellar absorption extending bluewards until -60 km s^{-1} , including another distinct (weak) absorption component near $v_{\text{helio}} = -40 \text{ km s}^{-1}$ (Fig. 14). The strong $\text{C II } \lambda 1334.5 \text{ \AA}$ and $\text{Si III } \lambda 1206.5 \text{ \AA}$ lines show additional weak absorption between -30 km s^{-1} and zero velocities, but without a clear component structure.

¹¹ <http://www.galex.caltech.edu>

¹² <http://galex.stsci.edu/GalexView>

¹³ Orbiting and Retrievable Far and Extreme Ultraviolet Spectrometer / Berkeley Extreme and Far-ultraviolet Spectrometer

¹⁴ <http://www.g-vo.org>

¹⁵ <http://dc.g-vo.org/theossa>

¹⁶ <http://sci.esa.int/gaia>

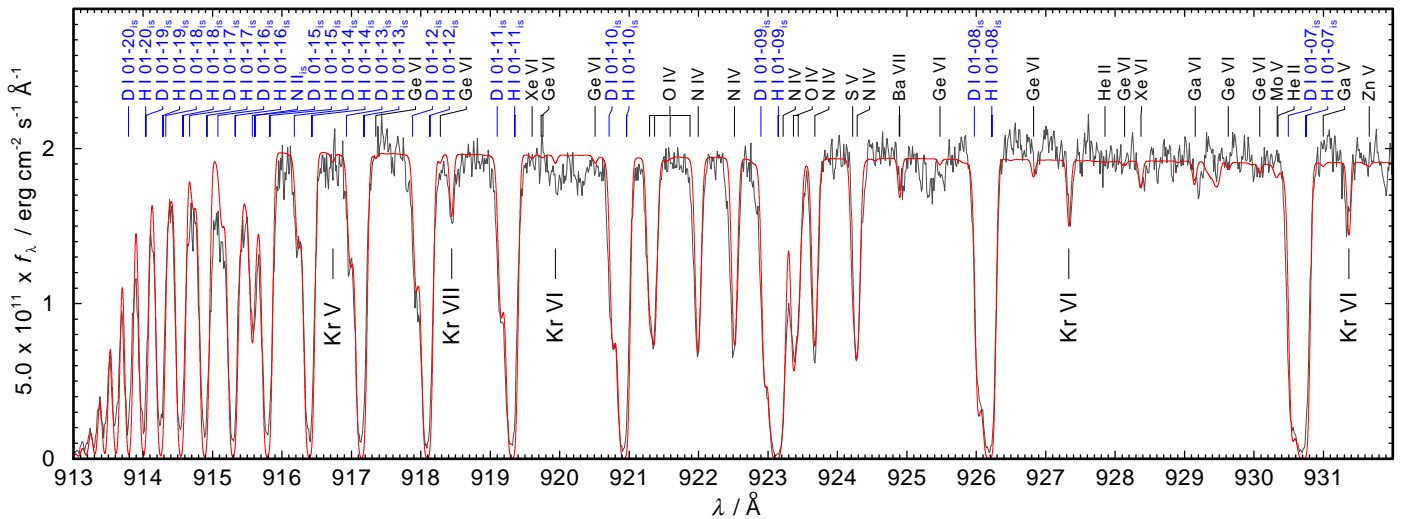


Fig. 12. Section of the FUSE observation (shifted to rest wavelengths) compared with our final synthetic spectrum ($T_{\text{eff}} = 70\,000\text{ K}$, $\log g = 7.5$). Prominent stellar and interstellar (IS, blue) lines are indicated.

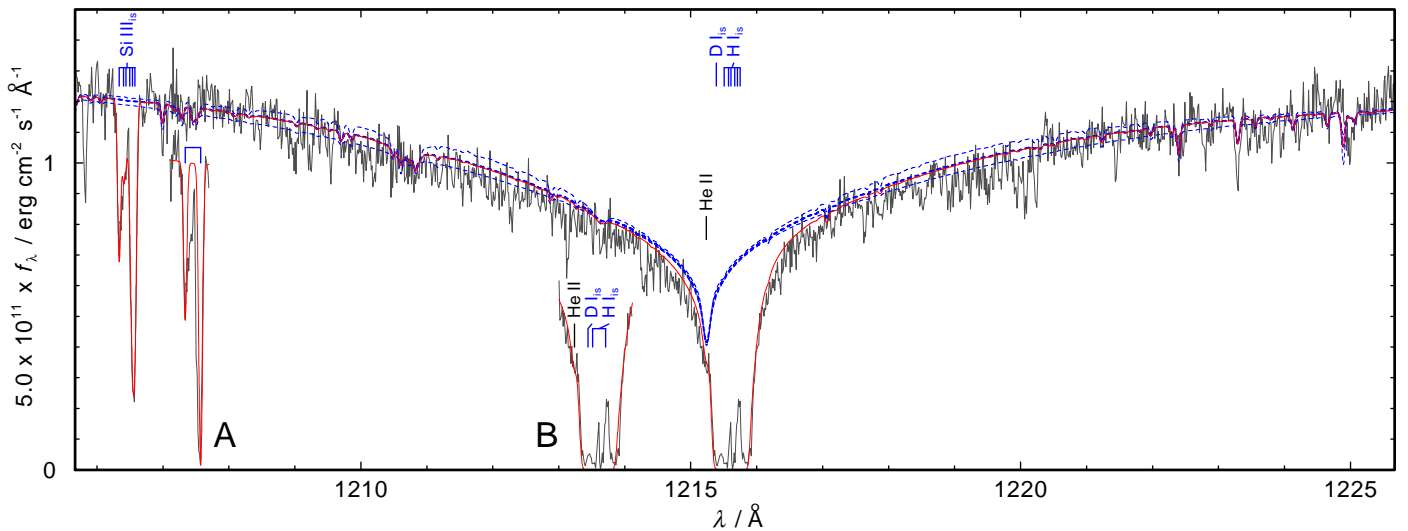


Fig. 13. Section of the STIS observation around $L\alpha$, compared with our final synthetic spectrum (thick, red, $T_{\text{eff}} = 70\,000\text{ K}$, $\log g = 7.5$). The dashed, blue lines are the pure photospheric model-atmosphere spectra ($T_{\text{eff}} = 70\,000\text{ K}$, $\log g = 7.0, 7.5, 8.0$), i.e., no interstellar line absorption is applied. See text for the description of inserts A and B.

The H I Lyman series absorption can also be best fit with two neutral gas components at $+15$ and -40 km s^{-1} , with a total column density of $N_{\text{H I}} = 1.5 \times 10^{18}\text{ cm}^{-2}$.

In the metal ions, the satellite component at -40 km s^{-1} is relatively narrow with a b -value of just 2.5 km s^{-1} . The simultaneous presence of weak C II, Si II, Si III, and H I absorption (and possibly O VI; Fig. 14), together with the narrow line shape, indicates a relatively compact, low-column density gas structure with multiphase gas that causes the absorption at negative velocities.

To estimate the contribution of the circumstellar material to the ISM absorption in the LOS toward RE 0503–289 and RE 0457–281, we estimated the densities of planetary nebulae (PNe) that were ejected at the end of the AGB phases of both stars. We assumed expansion velocities of $v_{\text{exp}} = 20\text{ km s}^{-1}$. Because of the very long post-AGB times, these PNe have swept up all stellar material ejected in the slow ($\approx 10\text{ km s}^{-1}$) AGB-wind phase before, and their so-called radii indicate the maximum distance from the star that ejected material would have reached.

Table 17 summarizes radii, volumes, masses, and densities of the expected PNe. The estimated column densities are orders of magnitude lower than those that are necessary to reproduce the observation, even if RE 0503–289 lies beyond the circumstellar material of RE 0457–281. However, the ejected PN material may have compressed accelerated ambient interstellar gas, so that the -40 km s^{-1} component toward RE 0503–289 may be a result of the interaction between circumstellar and interstellar material at the interface between both components.

9. Results and conclusions

We reanalyzed the effective temperature and surface gravity and determined $T_{\text{eff}} = 70\,000 \pm 2000\text{ K}$ and $\log g = 7.5 \pm 0.1$. This verifies the results of Dreizler & Werner (1996) within improved, rather small, error limits.

For precise NLTE spectral analyses, reliable transition probabilities are required, not only for lines that are identified in the observation, but also for the complete model atoms that are considered in the model-atmosphere calculations. Therefore, our

Table 16. Ionic column densities (in cm^{-2}) and radial velocities (in km s^{-1}) in interstellar clouds in the line of sight toward RE 0503–289.

C II λ 1036.3 Å C II λ 1334.5 Å		C III λ 977.0 Å		N II λ 1084.0 Å		O I λ 988.6 Å O I λ 988.7 Å O I λ 988.8 Å		O VI λ 1031.9 Å O VI λ 1037.6 Å		Si II λ 1260.4 Å Si II λ 1526.7 Å		Si III λ 1206.5 Å	
N	v_{rad}	N	v_{rad}	N	v_{rad}	N	v_{rad}	N	v_{rad}	N	v_{rad}	N	v_{rad}
7.0×10^{13}	+18.0	8.0×10^{12}	+17.0	3.0×10^{13}	+17.0	8.0×10^{13}	+19.0	1.0×10^{13}	+17.0	5.0×10^{12}	+17.0	4.0×10^{12}	+19.0
7.0×10^{13}	+8.0	8.0×10^{12}	+7.0	3.0×10^{13}	+7.0	5.0×10^{13}	+9.0	1.0×10^{13}	+7.0	5.0×10^{12}	+9.0	4.0×10^{12}	+9.0
1.0×10^{13}	−0.5	8.0×10^{12}	−0.5	1.0×10^{13}	−0.5	5.0×10^{13}	−0.5	1.0×10^{13}	−0.5	1.5×10^{12}	−0.5	6.0×10^{11}	−0.5
9.0×10^{12}	−14.5	6.0×10^{12}	−14.5	7.0×10^{12}	−14.5	4.0×10^{13}	−14.5	9.0×10^{12}	−14.5	5.0×10^{11}	−14.5	4.5×10^{11}	−14.5
9.0×10^{12}	−24.5	4.0×10^{12}	−24.5	4.0×10^{12}	−24.5	5.0×10^{13}	−24.5	9.0×10^{12}	−24.5	2.5×10^{11}	−24.5	8.0×10^{11}	−24.5
2.2×10^{13}	−40.5	6.0×10^{12}	−40.5	1.5×10^{13}	−40.5	4.0×10^{13}	−40.5	1.7×10^{13}	−40.5	1.5×10^{12}	−40.5	1.9×10^{12}	−40.5

Table 17. Parameters to estimate the circumstellar column densities around RE 0503–289 and RE 0457–281 owing to their AGB mass loss.

	RE 0503–289	RE 0457–281
Post-AGB age / 10^6 a	0.80 ^a	1.2 ^b
$R_{\text{max}}^{\text{PN}}$ / cm	5.0×10^{19} ^c	7.5×10^{19} ^c
$R_{\text{max}}^{\text{PN}}$ / pc	16.4	24.5
$V_{\text{max}}^{\text{PN}}$ / cm^3	5.3×10^{59}	1.8×10^{60}
$M_{\text{ZAMS}}^{\text{d}}$ / M_{\odot}	1.0 ^a	2.5 ^b
M_{final} / M_{\odot}	0.514 ^e	0.660 ^f
AGB mass loss / M_{\odot}	0.486	1.840
AGB mass loss / $M_{\text{H I}}$	5.8×10^{56}	2.2×10^{57}
Column density ^g / cm^{-2}	5.4×10^{15}	9.2×10^{15}

Notes. ^(a) Althaus et al. (2009) ^(b) Renedo et al. (2010) ^(c) $v_{\text{exp}} = 20 \text{ km s}^{-1}$ assumed ^(d) zero-age main sequence ^(e) Werner et al. (2015) ^(f) this paper ^(g) circumstellar, assumed location of swept up material within 0.9 - 1.0 $R_{\text{max}}^{\text{PN}}$

new computation of a complete set of transition probabilities for Kr IV–VII transition probabilities was a prerequisite for an improved NLTE spectral analysis. The new data enabled us to construct a more realistic Kr model atom. We improved the previous determination of the Kr abundance in RE 0503–289 (Werner et al. 2012b), taking these oscillator strengths into consideration.

In addition to the already known 15 Kr VI–VII lines in the observed high-resolution UV spectrum of RE 0503–289 (Werner et al. 2012b), we identified one Kr VI line and, for the first time in this star, ten lines of Kr V. Our synthetic line profiles reproduce well the observation at a photospheric Kr abundance of $2.5 \times 10^{-4} - 1.0 \times 10^{-3}$ ($\log \text{Kr} = -3.3 \pm 0.3$). This is 2300–9200 times the solar abundance (Grevesse et al. 2015). This highly super-solar Kr abundance goes along with the high abundances of other trans-iron elements in RE 0503–289 (Fig. 16). The Kr V–VII ionization equilibrium is well reproduced (Figs. 5, 8).

Iron is the only element in Fig. 16 with an upper abundance limit ($\text{Fe}/\text{He} < 10^{-6}$ by number, about a hundredth of the solar abundance, Scott et al. 2015a). Barstow et al. (2000) determined this value by a co-addition (in the velocity space) of the nine Fe V lines that were predicted to be strongest in the HST/GHRS spectrum. In Fig 17, we compare theoretical line profiles of the most prominent Fe V lines in the FUSE and HST/STIS wavelength range to the observation. The upper limit for the Fe abundance of 0.01 times solar is verified. Therefore, the reason why the

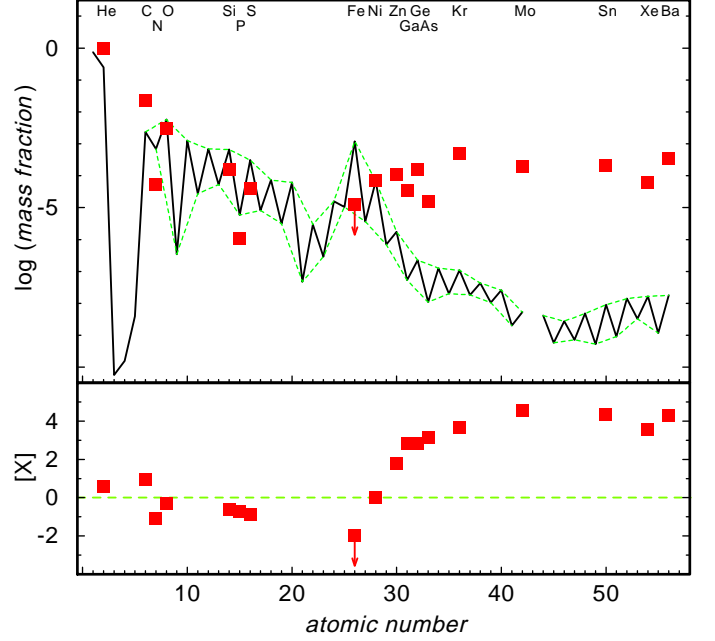


Fig. 16. Solar abundances (Asplund et al. 2009; Scott et al. 2015b,a; Grevesse et al. 2015, thick line; the dashed lines connect the elements with even and odd atomic numbers) compared with the determined photospheric abundances of RE 0503–289 (red squares, Dreizler & Werner 1996; Rauch et al. 2014a, 2015b, 2012, 2015a, 2014b, and this work). The uncertainties of the WD abundances are about 0.2 dex, in general. For Fe, the arrow indicates the upper limit. Top panel: Abundances given as logarithmic mass fractions. Bottom panel: Abundance ratios to respective solar values, $[X]$ denote $\log(\text{fraction}/\text{solar fraction})$ of species X. The dashed, green line indicates solar abundances.

Ni/Fe abundance ratio is much higher compared to other post-AGB stars remains unexplained (see Barstow et al. 2000).

Acknowledgements. TR and DH are supported by the German Aerospace Center (DLR, grants 05 OR 1507 and 50 OR 1501, respectively). The GAVO project had been supported by the Federal Ministry of Education and Research (BMBF) at Tübingen (05 AC 6 VTB, 05 AC 11 VTB) and is funded at Heidelberg (05 AC 11 VH3). Financial support from the Belgian FRS-FNRS is also acknowledged. PQ is research director of this organization. Some of the data presented in this paper were obtained from the Mikulski Archive for Space Telescopes (MAST). STScI is operated by the Association of Universities for Research in Astronomy, Inc., under NASA contract NAS5-26555. Support for MAST for non-HST data is provided by the NASA Office of Space Science via grant NNX09AF08G and by other grants and contracts. We thank Ralf Napiwotzki for putting the reduced ESO/VLT spectra at our disposal, Monica Raineri who sent us the electronic versions of the Kr IV (Bredice et al. 2000) and Kr V (Raineri et al. 2012) $\log gf$ data, and Liang Liang who provided the Kr VII data (Liang et al. 2013). This work used the profile-fitting procedure, OWENS, that was developed by M. Lemoine and the FUSE French Team.

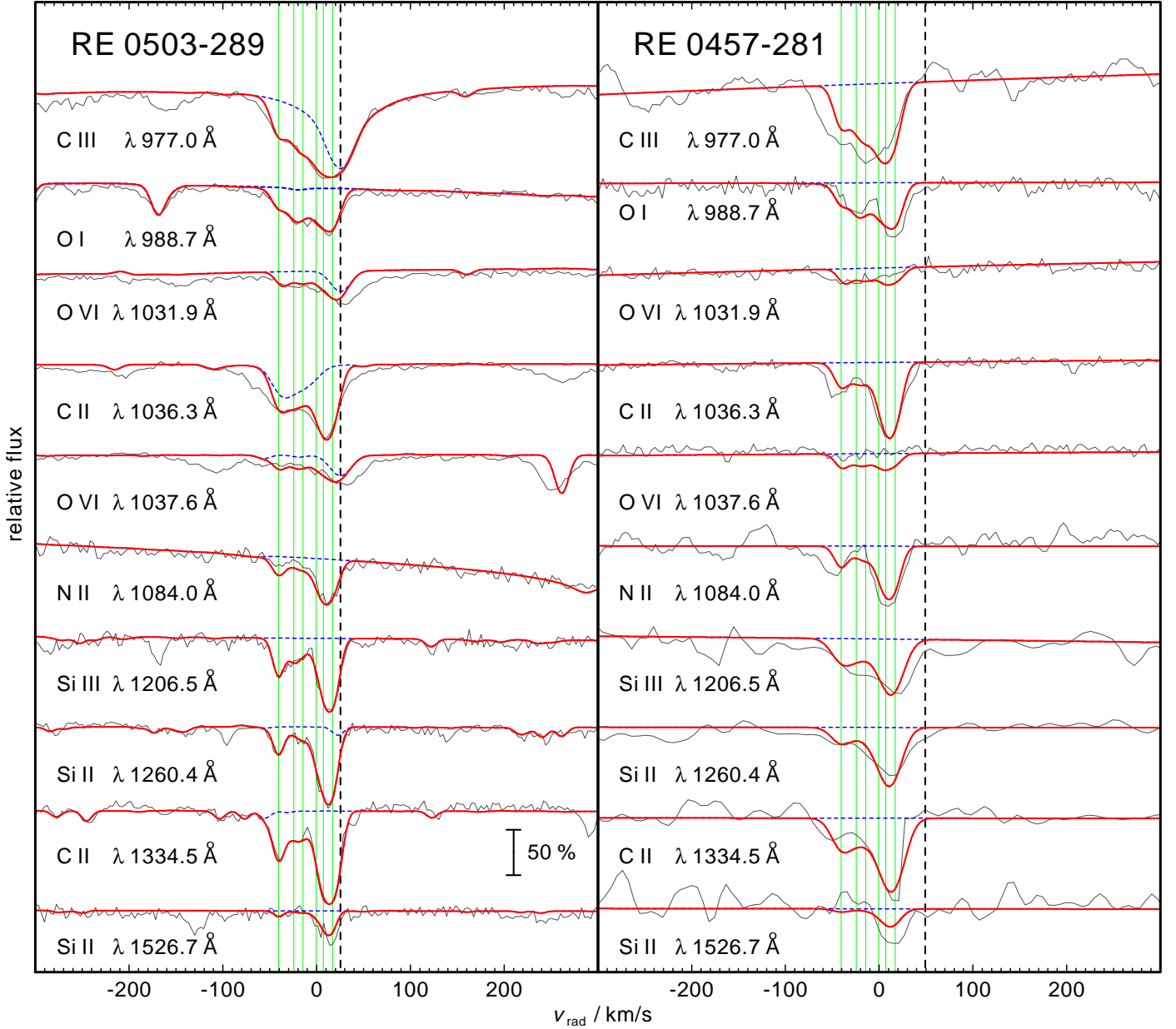


Fig. 14. Sections of the FUSE, STIS, and IUE observations around interstellar lines compared with our synthetic spectra for RE 0503–289 (left) and RE 0457–281 (right). The pure stellar model spectra are shown with dashed, blue lines. The vertical lines indicate the assumed clouds’ velocities given in Table 16. The dashed, vertical lines in each panel show the radial velocities of the two stars.

This research has made use of NASA’s Astrophysics Data System and the SIMBAD database, operated at CDS, Strasbourg, France. The TheoSSA service (<http://dc.g-vo.org/theoSSA>) used to retrieve theoretical spectra for this paper and the TOSS service (<http://dc.g-vo.org/TOSS>) that provides weighted oscillator strengths and transition probabilities were constructed as part of the activities of the German Astrophysical Virtual Observatory.

References

- Althaus, L. G., Panei, J. A., Miller Bertolami, M. M., et al. 2009, *ApJ*, 704, 1605
 Asplund, M., Grevesse, N., Sauval, A. J., & Scott, P. 2009, *ARA&A*, 47, 481
 Badnell, N. R. 2011, *Computer Physics Communications*, 182, 1528
 Barnard, A. J., Cooper, J., & Smith, E. W. 1974, *J. Quant. Spec. Radiat. Transf.*, 14, 1025
 Barstow, M. A., Dreizler, S., Holberg, J. B., et al. 2000, *MNRAS*, 314, 109
 Bredice, F., Raineri, M., Almandos, J. R., Gallardo, M., & Trigueiros, A. G. 2000, *J. Quant. Spec. Radiat. Transf.*, 65, 805
 Cowan, R. D. 1981, *The theory of atomic structure and spectra* (Berkeley, CA, University of California Press)
 Cowley, C. R. 1970, *The theory of stellar spectra* (Gordon & Breach, New York)
 Cowley, C. R. 1971, *The Observatory*, 91, 139
 Cutri, R. M., Skrutskie, M. F., van Dyk, S., et al. 2003, *VizieR Online Data Catalog*, 2246
 Demers, S., Beland, S., Kibblewhite, E. J., Irwin, M. J., & Nithakorn, D. S. 1986, *AJ*, 92, 878
 Dreizler, S. 1999, *A&A*, 352, 632
 Dreizler, S. & Werner, K. 1996, *A&A*, 314, 217
 Dupuis, J., Vennes, S., Bowyer, S., Pradhan, A. K., & Thejll, P. 1995, *ApJ*, 455, 574
 Faedi, F., West, R. G., Burleigh, M. R., Goad, M. R., & Hebb, L. 2011, *MNRAS*, 410, 899
 Farias, E. E., Raineri, M., Gallardo, M., et al. 2011, *J. Quant. Spec. Radiat. Transf.*, 112, 2463
 Fitzpatrick, E. L. 1999, *PASP*, 111, 63
 Gianninas, A., Bergeron, P., Dupuis, J., & Ruiz, M. T. 2010, *ApJ*, 720, 581
 Gianninas, A., Bergeron, P., & Ruiz, M. T. 2011, *ApJ*, 743, 138
 Grevesse, N., Scott, P., Asplund, M., & Sauval, A. J. 2015, *A&A*, 573, A27
 Gudennavar, S. B., Bubbly, S. G., Preethi, K., & Murthy, J. 2012, *ApJS*, 199, 8
 Heber, U., Hunger, K., Jonas, G., & Kudritzki, R. P. 1984, *A&A*, 130, 119

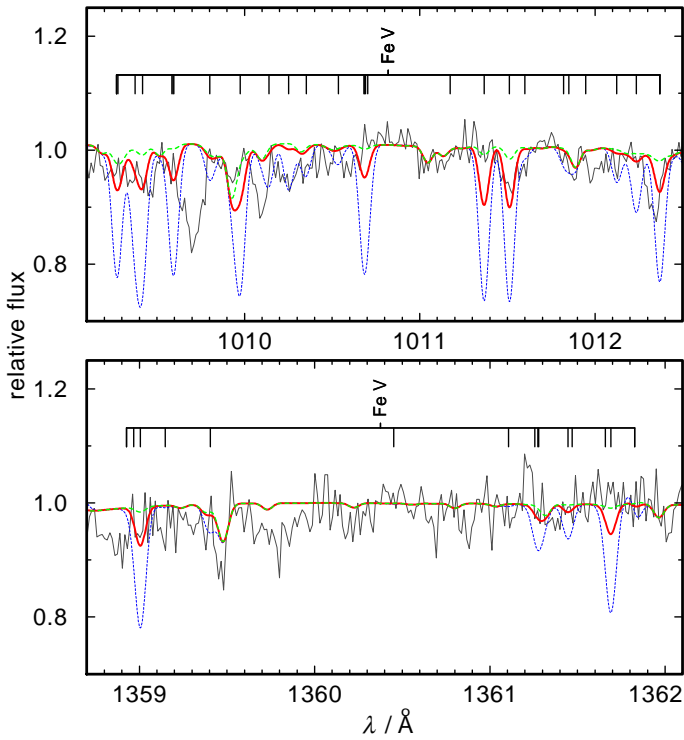


Fig. 17. Sections of the FUSE (top panel) and HST/STIS (bottom) spectra compared with synthetic spectra ($T_{\text{eff}} = 70\,000\text{ K}$, $\log g = 7.5$) that were calculated with Fe abundances of 1.3×10^{-5} (dashed, green), 1.3×10^{-4} (full, red), and 1.3×10^{-3} (dashed, blue) (about 0.01, 0.1, 1 times solar, respectively). Fe v lines are indicated.

Rauch, T., Werner, K., Quinet, P., & Kruk, J. W. 2014b, *A&A*, 566, A10
Rauch, T., Werner, K., Quinet, P., & Kruk, J. W. 2015b, *A&A*, 577, A6
Renedo, I., Althaus, L. G., Miller Bertolami, M. M., et al. 2010, *ApJ*, 717, 183
Rezende, D. C. J., Borges, F. O., Cavalcanti, G. H., et al. 2010, *J. Quant. Spec. Radiat. Transf.*, 111, 2000
Saloman, E. B. 2007, *Journal of Physical and Chemical Reference Data*, 36, 215
Schlafly, E. F. & Finkbeiner, D. P. 2011, *ApJ*, 737, 103
Schlegel, D. J., Finkbeiner, D. P., & Davis, M. 1998, *ApJ*, 500, 525
Schoening, T. & Butler, K. 1989, *A&AS*, 78, 51
Scott, P., Asplund, M., Grevesse, N., Bergemann, M., & Sauval, A. J. 2015a, *A&A*, 573, A26
Scott, P., Grevesse, N., Asplund, M., et al. 2015b, *A&A*, 573, A25
Seaton, M. J. 1962, in *Atomic and Molecular Processes*, ed. D. R. Bates (Academic Press, New York), 375
Vallerga, J. V., Vedder, P. W., & Welsh, B. Y. 1993, *ApJ*, 414, L65
van Regemorter, H. 1962, *ApJ*, 136, 906
Vennes, S., Dupuis, J., Bowyer, S., et al. 1994, *ApJ*, 421, L35
Vennes, S., Dupuis, J., Chayer, P., et al. 1998, *ApJ*, 500, L41
Victor, G. A. & Taylor, W. R. 1983, *Atomic Data and Nuclear Data Tables*, 28, 107
Werner, K., Deetjen, J. L., Dreizler, S., et al. 2003, in *Astronomical Society of the Pacific Conference Series*, Vol. 288, *Stellar Atmosphere Modeling*, ed. I. Hubeny, D. Mihalas, & K. Werner, 31
Werner, K., Dreizler, S., & Rauch, T. 2012a, *TMAP: Tübingen NLTE Model-Atmosphere Package*, Astrophysics Source Code Library
Werner, K., Rauch, T., & Kruk, J. W. 2015, *A&A*, 582, A94
Werner, K., Rauch, T., Ringat, E., & Kruk, J. W. 2012b, *ApJ*, 753, L7
Ziegler, M., Rauch, T., Werner, K., Köppen, J., & Kruk, J. W. 2012, *A&A*, 548, A109

Hébrard, G., Friedman, S. D., Kruk, J. W., et al. 2002, *Planet. Space Sci.*, 50, 1169
Hébrard, G. & Moos, H. W. 2003, *ApJ*, 599, 297
Hoare, M. G., Drew, J. E., & Denby, M. 1993, *MNRAS*, 262, L19
Holberg, J. B., Barstow, M. A., & Sion, E. M. 1998, *ApJS*, 119, 207
Hubeny, I., Hummer, D. G., & Lanz, T. 1994, *A&A*, 282, 151
Hummer, D. G. & Mihalas, D. 1988, *ApJ*, 331, 794
Johnson, W. R., Kolb, D., & Huang, K.-N. 1983, *Atomic Data and Nuclear Data Tables*, 28, 333
Kalberla, P. M. W., Burton, W. B., Hartmann, D., et al. 2005, *A&A*, 440, 775
Liang, L., Gao, W.-j., & Zhou, C. 2013, *Can. J. Phys.*, 91, 554
Marsh, M. C., Barstow, M. A., Buckley, D. A., et al. 1997, *MNRAS*, 286, 369
Mason, K. O., Hassall, B. J. M., Bromage, G. E., et al. 1995, *MNRAS*, 274, 1194
Mason, K. O., Hassall, B. J. M., Bromage, G. E., et al. 1996, *VizieR Online Data Catalog*, 727
McCook, G. P. & Sion, E. M. 1999a, *ApJS*, 121, 1
McCook, G. P. & Sion, E. M. 1999b, *VizieR Online Data Catalog*, 3210, 0
Napiwotzki, R., Christlieb, N., Drechsel, H., et al. 2001, *Astronomische Nachrichten*, 322, 411
Napiwotzki, R., Christlieb, N., Drechsel, H., et al. 2003, *The Messenger*, 112, 25
Pagan, C. J. B., Raineri, M., Bredice, F., et al. 1996, *J. Quant. Spec. Radiat. Transf.*, 55, 163
Pauli, E.-M., Napiwotzki, R., Heber, U., Altmann, M., & Odenkirchen, M. 2006, *A&A*, 447, 173
Pounds, K. A., Allan, D. J., Barber, C., et al. 1993, *MNRAS*, 260, 77
Pounds, K. A. & et al. 1993, *VizieR Online Data Catalog*, 726
Quinet, P., Palmeri, P., Biémont, E., et al. 2002, *J. Alloys Comp.*, 344, 255
Quinet, P., Palmeri, P., Biémont, E., et al. 1999, *MNRAS*, 307, 934
Raineri, M., Fariñas, E. E., Souza, J. O., et al. 2014, *J. Quant. Spec. Radiat. Transf.*, 148, 90
Raineri, M., Gallardo, M., Pagan, C. J. B., Trigueiros, A. G., & Reyna Almandos, J. 2012, *J. Quant. Spec. Radiat. Transf.*, 113, 1612
Rauch, T. & Deetjen, J. L. 2003, in *Astronomical Society of the Pacific Conference Series*, Vol. 288, *Stellar Atmosphere Modeling*, ed. I. Hubeny, D. Mihalas, & K. Werner, 103
Rauch, T., Dreizler, S., & Wolff, B. 1998, *A&A*, 338, 651
Rauch, T., Quinet, P., Hoyer, D., et al. 2015a, *ArXiv e-prints* 1512.07525
Rauch, T., Werner, K., Biémont, E., Quinet, P., & Kruk, J. W. 2012, *A&A*, 546, A55
Rauch, T., Werner, K., Quinet, P., & Kruk, J. W. 2014a, *A&A*, 564, A41

Table 2. Radial parameters (in cm^{-1}) adopted for the calculations in Kr iv.

Configuration	Parameter	HFR	Fitted	Ratio	Note ^a
Even parity					
4p ³	E_{av}	31247	30541		
	$F^2(4p,4p)$	63340	56159	0.887	
	α	0	−151		
	ζ_{4p}	4216	4645	1.102	
4p ² 5p	E_{av}	263829	253120		
	$F^2(4p,4p)$	65722	52042	0.792	
	α	0	−131		
	ζ_{4p}	4599	4674	1.016	
	ζ_{5p}	933	1116	1.196	
	$F^2(4p,5p)$	18258	15003	0.822	
	$G^0(4p,5p)$	4385	3446	0.786	
	$G^2(4p,5p)$	5522	3270	0.592	
Odd parity					
4s4p ⁴	E_{av}	170290	161670		
	$F^2(4p,4p)$	63371	55784	0.880	
	α	0	44		
	ζ_{4p}	4226	4517	1.069	
	$G^1(4s,4p)$	85304	70258	0.824	
4p ² 4d	E_{av}	209261	200718		
	$F^2(4p,4p)$	64336	59065	0.918	
	α	0	−901		
	ζ_{4p}	4393	4761	1.084	
	ζ_{4d}	212	212	1.000	F
	$F^2(4p,4d)$	47236	37274	0.789	
	$G^1(4p,4d)$	56206	44834	0.798	
	$G^3(4p,4d)$	34521	26906	0.779	
4p ² 5d	E_{av}	316350	305188		
	$F^2(4p,4p)$	65754	59179	0.900	F
	α	0	0		F
	ζ_{4p}	4592	4822	1.050	
	ζ_{5d}	71	71	1.000	F
	$F^2(4p,5d)$	13113	9803	0.748	
	$G^1(4p,5d)$	9555	5756	0.602	
	$G^3(4p,5d)$	6550	2767	0.422	
4p ² 5s	E_{av}	226731	219299		
	$F^2(4p,4p)$	65231	56784	0.871	
	α	0	0		F
	ζ_{4p}	4540	3540	0.780	
	$G^1(4p,5s)$	6715	4864	0.724	
4p ² 6s	E_{av}	320594	308931		
	$F^2(4p,4p)$	74046	51830	0.700	
	α	0	0		F
	ζ_{4p}	4609	4377	0.950	
	$G^1(4p,6s)$	2039	1454	0.713	
4s4p ⁴ –4p ² 4d	$R^1(4p4p;4s4d)$	67039	53177	0.793	
4p ² 4d–4p ² 5s	$R^2(4p4d;4p5s)$	−11024	−8360	0.758	R
	$R^1(4p4d;4p5s)$	−3424	−2597	0.758	R
4p ² 4d–4p ² 6s	$R^2(4p4d;4p6s)$	−5593	−5034	0.900	F
	$R^1(4p4d;4p6s)$	−2444	−2199	0.900	F

^a F: Fixed parameter value; R: ratios of these parameters had been fixed in the fitting process.

Table 3. Radial parameters (in cm^{-1}) adopted for the calculations in Kr v.

Configuration	Parameter	HFR	Fitted	Ratio	Note ^a
Even parity					
4p ²	E_{av}	23408	23750		
	$F^2(4p,4p)$	66066	57912	0.877	
	α	0	−98		
4p5p	ζ_{4p}	4645	5105	1.099	
	E_{av}	300733	291773		
	ζ_{4p}	5032	4888	0.971	
	ζ_{5p}	1264	1182	0.935	
	$F^2(4p,5p)$	21662	20479	0.945	
	$G^0(4p,5p)$	5328	4511	0.847	
	$G^2(4p,5p)$	6697	5667	0.846	
4s4p ² 4d	E_{av}	346630	346415		
4p ⁴	E_{av}	320528	322649		
Odd parity					
4s4p ³	E_{av}	159136	158128		
	$F^2(4p,4p)$	66074	50513	0.765	
	α	0	0		F
	ζ_{4p}	4649	5828	1.254	
4p4d	$G^1(4s,4p)$	88424	72266	0.817	
	E_{av}	219306	213693		
	ζ_{4p}	4799	4394	0.915	
	ζ_{4d}	275	275	1.000	F
	$F^2(4p,4d)$	52397	44934	0.858	
	$G^1(4p,4d)$	63320	49841	0.787	
	$G^3(4p,4d)$	39214	45038	1.149	
4p5d	E_{av}	364462	352723		
	ζ_{4p}	5025	4836	0.963	
	ζ_{5d}	102	102	1.000	F
	$F^2(4p,5d)$	16176	9684	0.599	
	$G^1(4p,5d)$	10523	8633	0.820	
	$G^3(4p,5d)$	7496	6263	0.836	
4p5s	E_{av}	256661	251657		
	ζ_{4p}	4968	5734	1.154	
	$G^1(4p,5s)$	7540	4673	0.620	
4p6s	E_{av}	377119	365301		
	ζ_{4p}	5046	5334	1.057	
	$G^1(4p,6s)$	2394	2335	0.975	

^a F: Fixed parameter value.

Table 4. Radial parameters (in cm^{-1}) adopted for the calculations in Kr VI.

Configuration	Parameter	HFR	Fitted	Ratio	Note ^a
Odd parity					
4p	E_{av}	15431	15919		
	ζ_{4p}	5091	5546	1.089	
5p	E_{av}	337490	329220		
	ζ_{5p}	1617	1767	1.093	
4s4p4d	E_{av}	350565	351918		
	ζ_{4p}	5220	5415	1.037	
	ζ_{4d}	346	346	1.000	F
	$F^2(4p,4d)$	57038	50496	0.885	
	$G^1(4s,4p)$	92075	72188	0.784	
	$G^2(4s,4d)$	49592	43311	0.873	
	$G^1(4p,4d)$	69847	57056	0.817	
	$G^3(4p,4d)$	43533	34997	0.804	
	E_{av}	305114	305873		
	$F^2(4p,4p)$	68581	61621	0.899	
4p ³	α	0	304		
	ζ_{4p}	5091	5691	1.118	
Even parity					
4s4p ²	E_{av}	147173	148647		
	$F^2(4p,4p)$	68576	61628	0.899	
	α	0	110		
	ζ_{4p}	5090	5666	1.113	
	$G^1(4s,4p)$	91343	77789	0.852	
4s ² 4d	E_{av}	228002	226689		
	ζ_{4d}	338	431	1.277	
4s ² 5s	E_{av}	286862	285751		
4s4p4f	E_{av}	506792	501684		
	ζ_{4p}	5404	5404	1.000	F
	ζ_{4f}	6	6	1.000	F
	$F^2(4p,4f)$	37406	33665	0.900	F
	$G^1(4s,4p)$	93167	83850	0.900	F
	$G^3(4s,4f)$	19489	17540	0.900	F
	$G^2(4p,4f)$	28677	25809	0.900	F
	$G^4(4p,4f)$	19236	17313	0.900	F
	E_{av}	463187	466007		
4s4p5p	ζ_{4p}	5473	5110	0.934	
	ζ_{5p}	1614	1614	1.000	F
	$F^2(4p,5p)$	24821	22172	0.893	
	$G^1(4s,4p)$	93623	86030	0.919	
	$G^1(4s,5p)$	8886	11320	1.274	
	$G^0(4p,5p)$	5988	5531	0.924	
	$G^2(4p,5p)$	7695	3406	0.443	
	E_{av}	499443	500231		
	$F^2(4p,4p)$	69165	47563	0.688	
4p ² 4d	α	0	0		F
	ζ_{4p}	5218	5218	1.000	F
	ζ_{4d}	355	355	1.000	F
	$F^2(4p,4d)$	57487	62738	1.091	
	$G^1(4p,4d)$	70632	63569	0.900	F
	$G^3(4p,4d)$	44022	39619	0.900	F

^a F: Fixed parameter value.

Table 5. Radial parameters (in cm^{-1}) adopted for the calculations in Kr VII.

Configuration	Parameter	HFR	Fitted	Ratio	Note ^a
Even parity					
4s ²	E _{av}	8227	8218		
4p ²	E _{av}	289178	291671		
	F ² (4p,4p)	70911	62322	0.879	
	α	0	422		
	ζ_{4p}	5539	6051	1.093	
4s4d	E _{av}	353888	356691		
	ζ_{4d}	409	465	1.139	
	G ² (4s,4d)	53902	44704	0.829	
4s5d	E _{av}	579173	581325		
	ζ_{5d}	177	187	1.055	
	G ² (4s,5d)	11322	9859	0.871	
4s6d	E _{av}	683676	695114		
	ζ_{6d}	93	37	0.402	
	G ² (4s,6d)	4620	4581	0.992	
4s5s	E _{av}	440196	443108		
	G ⁰ (4s,5s)	6376	5370	0.842	
4s6s	E _{av}	615445	617416		
	G ⁰ (4s,6s)	2147	1678	0.781	
4p4f	E _{av}	672682	676175		
	ζ_{4p}	5812	5961	1.026	
	ζ_{4f}	9	9	1.000	F
	F ² (4p,4f)	46055	41087	0.892	
	G ² (4p,4f)	38271	36641	0.957	
	G ⁴ (4p,4f)	25858	26345	1.019	
Odd parity					
4s4p	E _{av}	135333	138188		
	ζ_{4p}	5543	6129	1.106	
	G ¹ (4s,4p)	94111	81424	0.865	
4s5p	E _{av}	495526	497735		
	ζ_{5p}	1980	2043	1.032	
	G ¹ (4s,5p)	9906	8373	0.845	
4s6p	E _{av}	641915	641868		
	ζ_{6p}	956	1194	1.249	
	G ¹ (4s,6p)	3572	3319	0.929	
4s4f	E _{av}	526025	528712		
	ζ_{4f}	9	9	1.000	F
	G ³ (4s,4f)	26755	25936	0.969	
4s5f	E _{av}	654124	658035		
	ζ_{5f}	5	5	1.000	F
	G ³ (4s,5f)	10833	9794	0.904	
4s6f	E _{av}	723392	729438		
	ζ_{6f}	3	3	1.000	F
	G ³ (4s,6f)	5366	4829	0.900	F
4p5s	E _{av}	589297	592304		
	ζ_{4p}	5854	5954	1.017	
	G ¹ (4p,5s)	9174	6377	0.695	
4p4d	E _{av}	497970	502593		
	ζ_{4p}	5652	6253	1.106	
	ζ_{4d}	417	417	1.000	F
	F ² (4p,4d)	60912	53229	0.874	
	G ¹ (4p,4d)	75244	64096	0.852	
	G ³ (4p,4d)	47132	39986	0.848	

^a F: Fixed parameter value.

Table 6. Comparison between available experimental and calculated energy levels in Kr IV. Energies are given in cm⁻¹.

E_{exp}^a	E_{calc}^b	ΔE	J	Leading components (in %) in LS coupling ^c
Odd parity				
0.0	0	0	1.5	95 4p ³ 4S
17037.6	17022	16	1.5	87 4p ³ 2D + 10 4p ³ 2P
18700.3	18716	-16	2.5	97 4p ³ 2D
31056.4	31067	-11	0.5	96 4p ³ 2P
33405.6	33395	11	1.5	85 4p ³ 2P + 10 4p ³ 2D
234827.9	234724	104	0.5	64 4p ² (3P)5p 2S + 19 4p ² (3P)5p 4D + 7 4p ² (3P)5p 4P
237445.1	237386	59	0.5	74 4p ² (3P)5p 4D + 23 4p ² (3P)5p 2S
238269.4	238363	-94	1.5	85 4p ² (3P)5p 4D + 8 4p ² (3P)5p 4P
241241.6	241222	20	2.5	92 4p ² (3P)5p 4D + 5 4p ² (3P)5p 4P
241802.6	241926	-123	1.5	31 4p ² (3P)5p 4P + 31 4p ² (3P)5p 2D + 15 4p ² (3P)5p 4S
243567.2	243565	2	0.5	90 4p ² (3P)5p 4P + 5 4p ² (3P)5p 2S
243898.8	244005	-107	1.5	40 4p ² (3P)5p 2D + 32 4p ² (3P)5p 4S + 14 4p ² (3P)5p 4P
244443.6	244324	120	3.5	93 4p ² (3P)5p 4D + 6 4p ² (1D)5p 2F
244465.9	244400	66	2.5	45 4p ² (3P)5p 4P + 30 4p ² (3P)5p 2D + 18 4p ² (1D)5p 2D
246612.9	246480	133	1.5	46 4p ² (3P)5p 4S + 42 4p ² (3P)5p 4P
249206.2	249357	-151	2.5	44 4p ² (3P)5p 2D + 44 4p ² (3P)5p 4P + 6 4p ² (1D)5p 2F
250173.8	250274	-100	1.5	72 4p ² (3P)5p 2P + 14 4p ² (1D)5p 2P + 7 4p ² (1D)5p 2D
250896.7	250834	63	0.5	80 4p ² (3P)5p 2P + 6 4p ² (3P)5p 2S
257142.7	257069	74	2.5	65 4p ² (1D)5p 2F + 32 4p ² (1D)5p 2D
258355.4	258340	15	1.5	61 4p ² (1D)5p 2D + 16 4p ² (1D)5p 2P + 15 4p ² (3P)5p 2D
258509.6	258606	-97	3.5	94 4p ² (1D)5p 2F + 6 4p ² (3P)5p 4D
258763.2	258951	-188	2.5	46 4p ² (1D)5p 2D + 25 4p ² (3P)5p 2D + 24 4p ² (1D)5p 2F
263160.1	263042	118	0.5	89 4p ² (1D)5p 2P + 7 4p ² (3P)5p 2P
265447.4	265352	95	1.5	60 4p ² (1D)5p 2P + 23 4p ² (3P)5p 2P + 8 4p ² (1D)5p 2D
278967.3	278973	-6	1.5	82 4p ² (1S)5p 2P
Even parity				
118761.5	118649	113	2.5	89 4s4p ⁴ 4P + 9 4p ² (3P)4d 4P
122426.5	122407	20	1.5	89 4s4p ⁴ 4P + 10 4p ² (3P)4d 4P
124109.7	124166	-56	0.5	88 4s4p ⁴ 4P + 10 4p ² (3P)4d 4P
145772.8	145859	-87	1.5	75 4s4p ⁴ 2D + 18 4p ² (1D)4d 2D
146644.7	146531	114	2.5	76 4s4p ⁴ 2D + 18 4p ² (1D)4d 2D
163445.1	163634	-189	1.5	49 4p ² (3P)4d 2P + 40 4s4p ⁴ 2P + 6 4p ² (1D)4d 2P
166160.9	166309	-148	0.5	41 4p ² (3P)4d 2P + 36 4s4p ⁴ 2P + 12 4s4p ⁴ 2S
172724.0	172614	110	1.5	93 4p ² (3P)4d 4F
173952.1	173919	33	0.5	62 4s4p ⁴ 2S + 20 4p ² (1D)4d 2S + 10 4p ² (3P)4d 2P
174105.7	173998	108	2.5	90 4p ² (3P)4d 4F + 7 4p ² (3P)4d 4D
176231.0	176126	105	3.5	91 4p ² (3P)4d 4F + 7 4p ² (3P)4d 4D
178877.0	178733	144	4.5	95 4p ² (3P)4d 4F
179228.3	179309	-81	2.5	39 4p ² (1D)4d 2F + 30 4p ² (3P)4d 2F + 26 4p ² (3P)4d 4D
180686.7	180516	170	0.5	96 4p ² (3P)4d 4D
180764.4	180685	79	3.5	51 4p ² (3P)4d 4D + 27 4p ² (1D)4d 2F + 16 4p ² (3P)4d 2F
181000.5	180838	162	1.5	93 4p ² (3P)4d 4D
182668.4	182642	26	2.5	63 4p ² (3P)4d 4D + 16 4p ² (1D)4d 2F + 14 4p ² (3P)4d 2F
186565.6	186599	-33	3.5	40 4p ² (3P)4d 4D + 30 4p ² (1D)4d 2F + 23 4p ² (3P)4d 2F
201424.2	202477	-1053	2.5	81 4p ² (3P)4d 4P + 8 4s4p ⁴ 4P + 5 4p ² (3P)5s 4P
202373.3	202475	-101	0.5	78 4p ² (3P)5s 4P + 14 4p ² (3P)4d 4P
204735.4	205934	-1198	0.5	65 4p ² (3P)4d 4P + 13 4p ² (3P)5s 4P + 7 4s4p ⁴ 4P
205214.5	203480	1735	1.5	56 4p ² (3P)4d 4P + 31 4p ² (3P)5s 4P + 6 4s4p ⁴ 4P
205399.6	205070	329	1.5	36 4s4p ⁴ 2P + 18 4p ² (3P)4d 2P + 16 4p ² (3P)4d 2D
207595.4	207884	-289	1.5	38 4p ² (3P)4d 2D + 20 4p ² (1S)4d 2D + 9 4s4p ⁴ 2P
208064.1	208344	-280	2.5	89 4p ² (3P)5s 4P
208920.0	208458	462	0.5	72 4p ² (3P)5s 2P + 10 4s4p ⁴ 2P + 7 4p ² (3P)4d 2P
210347.7	210562	-215	0.5	47 4p ² (1D)4d 2P + 29 4s4p ⁴ 2P + 9 4p ² (3P)4d 2P
211685.5	212142	-456	1.5	79 4p ² (3P)5s 2P + 7 4p ² (1D)4d 2P

Table 6. continued.

E_{exp}^a	E_{calc}^b	ΔE	J	Leading components (in %) in <i>LS</i> coupling ^c
211860.3	212328	−467	2.5	66 $4p^2(^3P)4d^2D$ + 22 $4p^2(^1S)4d^2D$
217416.6	217695	−279	2.5	53 $4p^2(^1D)4d^2D$ + 19 $4p^2(^1D)5s^2D$ + 11 $4p^2(^1S)4d^2D$
217558.6	217720	−162	1.5	50 $4p^2(^1D)4d^2D$ + 16 $4p^2(^1D)5s^2D$ + 14 $4p^2(^1D)4d^2P$
219988.5	219854	135	2.5	42 $4p^2(^3P)4d^2F$ + 36 $4p^2(^1D)4d^2F$ + 7 $4p^2(^1S)4d^2D$
221184.5	221062	122	3.5	58 $4p^2(^3P)4d^2F$ + 37 $4p^2(^1D)4d^2F$
223033.6	222402	631	1.5	37 $4p^2(^1D)4d^2P$ + 23 $4p^2(^3P)4d^2P$ + 14 $4p^2(^1D)4d^2D$
223313.0	224326	−1013	2.5	74 $4p^2(^1D)5s^2D$ + 15 $4p^2(^1D)4d^2D$ + 6 $4p^2(^1S)4d^2D$
225282.0	224146	1136	1.5	77 $4p^2(^1D)5s^2D$ + 11 $4p^2(^1D)4d^2D$ + 5 $4p^2(^3P)5s^2P$
231940.0	231608	332	2.5	47 $4p^2(^1S)4d^2D$ + 28 $4p^2(^3P)4d^2D$ + 7 $4p^2(^3P)4d^2F$
232807.4	232743	64	1.5	58 $4p^2(^1S)4d^2D$ + 34 $4p^2(^3P)4d^2D$
290606.4	290675	−69	1.5	74 $4p^2(^3P)5d^4F$ + 11 $4p^2(^3P)5d^4D$ + 6 $4p^2(^3P)5d^2P$
294367.2	294297	70	3.5	75 $4p^2(^3P)5d^4F$ + 21 $4p^2(^3P)5d^4D$
294632.3	294510	122	1.5	43 $4p^2(^3P)5d^2P$ + 22 $4p^2(^3P)5d^4D$ + 21 $4p^2(^3P)5d^4F$
295268.2	295191	77	0.5	76 $4p^2(^3P)5d^4D$ + 16 $4p^2(^3P)5d^2P$ + 6 $4p^2(^3P)5d^4P$
296713.3	296657	56	0.5	78 $4p^2(^3P)6s^4P$ + 16 $4p^2(^3P)6s^2P$
296954.4	297025	−71	2.5	74 $4p^2(^3P)5d^2F$ + 12 $4p^2(^3P)5d^4P$ + 8 $4p^2(^1D)5d^2F$
298052.4	298180	−128	3.5	57 $4p^2(^3P)5d^4D$ + 22 $4p^2(^3P)5d^4F$ + 11 $4p^2(^3P)5d^2F$
299255.8	299198	58	1.5	39 $4p^2(^3P)5d^4P$ + 29 $4p^2(^3P)6s^4P$ + 24 $4p^2(^3P)5d^4D$
299952.2	300115	−163	1.5	61 $4p^2(^3P)6s^4P$ + 24 $4p^2(^3P)5d^4P$ + 7 $4p^2(^3P)5d^4D$
300899.4	300958	−58	0.5	73 $4p^2(^3P)6s^2P$ + 16 $4p^2(^3P)6s^4P$ + 7 $4p^2(^3P)5d^2P$
301796.5	301785	12	3.5	73 $4p^2(^3P)5d^2F$ + 18 $4p^2(^3P)5d^4D$ + 6 $4p^2(^1D)5d^2G$
303231.3	303183	49	2.5	92 $4p^2(^3P)6s^4P$ + 7 $4p^2(^1D)6s^2D$
304543.7	304492	52	1.5	83 $4p^2(^3P)6s^2P$ + 8 $4p^2(^1D)6s^2D$ + 7 $4p^2(^3P)6s^4P$
315802.1	315805	−3	2.5	80 $4p^2(^1D)6s^2D$ + 12 $4p^2(^1D)5d^2D$ + 5 $4p^2(^3P)6s^4P$
315892.9	315912	−19	1.5	44 $4p^2(^1D)6s^2D$ + 41 $4p^2(^1D)5d^2P$ + 6 $4p^2(^1D)5d^2D$

^(a) From Saloman (2007).^(b) This work.^(c) Only the first three components that are larger than 5% are given.

Table 7. Comparison between available experimental and calculated energy levels in Kr v. Energies are given in cm^{-1} .

E_{exp}^a	E_{calc}^b	ΔE	J	Leading components (in %) in LS coupling ^c
Even parity				
0.0	−33	33	0	94 $4p^2\ ^3P$
3742.8	3782	−39	1	97 $4p^2\ ^3P$
7595.3	7630	−34	2	88 $4p^2\ ^3P$ + 9 $4p^2\ ^1D$
19722.9	19722	1	2	88 $4p^2\ ^1D$ + 9 $4p^2\ ^3P$
39203.9	39086	118	0	93 $4p^2\ ^1S$
278654.0	276953	1701	2	48 $4p^4\ ^3P$ + 41 $4s4p^24d\ ^3P$
278928.0	279073	−145	1	54 $4p5p\ ^1P$ + 42 $4p5p\ ^3D$
282439.0	281129	1310	1	45 $4p^4\ ^3P$ + 42 $4s4p^24d\ ^3P$ + 5 $4p5p\ ^3P$
283439.0	282245	1194	0	42 $4p^4\ ^3P$ + 39 $4s4p^24d\ ^3P$ + 12 $4p5p\ ^3P$
283559.0	283510	49	1	43 $4p5p\ ^3D$ + 26 $4p5p\ ^1P$ + 17 $4p5p\ ^3P$
283677.0	284044	−367	2	85 $4p5p\ ^3D$ + 8 $4p5p\ ^3P$
285981.0	285743	238	0	82 $4p5p\ ^3P$ + 7 $4p4\ ^3P$ + 5 $4s4p^24d\ ^3P$
288683.0	288408	275	1	67 $4p5p\ ^3P$ + 15 $4p5p\ ^1P$ + 11 $4p5p\ ^3D$
289297.0	288809	488	2	55 $4p^4\ ^1D$ + 28 $4s4p^24d\ ^1D$
289998.0	289534	464	3	98 $4p5p\ ^3D$
291138.0	290937	201	2	81 $4p5p\ ^3P$ + 10 $4p5p\ ^3D$
293705.0	293846	−141	1	88 $4p5p\ ^3S$ + 8 $4p5p\ ^3P$
296600.0	298028	−1428	2	91 $4p5p\ ^1D$ + 6 $4p5p\ ^3P$
307667.0	306878	789	0	91 $4p5p\ ^1S$
313479.1	316178	−2699	2	98 $4s4p^24d\ ^5P$
318440.7	317049	1391	1	99 $4s4p^24d\ ^5P$
319567.4	324289	−4722	0	52 $4p^4\ ^1S$ + 36 $4s4p^24d\ ^1S$
331254.6	330875	380	2	31 $4p^4\ ^3P$ + 27 $4s4p^24d\ ^3P$ + 22 $4s4p^24d\ ^3P$
356571.8	354502	2070	0	47 $4s4p^25s\ ^3P$ + 30 $4s4p^24d\ ^3P$
Odd parity				
129658.2	129841	−183	1	84 $4s4p^3\ ^3D$ + 11 $4p4d\ ^3D$
129779.3	129867	−88	2	82 $4s4p^3\ ^3D$ + 10 $4p4d\ ^3D$ + 6 $4s4p^3\ ^3P$
131016.4	131249	−232	3	88 $4s4p^3\ ^3D$ + 11 $4p4d\ ^3D$
147925.2	147849	76	0	87 $4s4p^3\ ^3P$ + 12 $4p4d\ ^3P$
148286.8	148187	100	1	83 $4s4p^3\ ^3P$ + 12 $4p4d\ ^3P$
148668.4	148398	270	2	73 $4s4p^3\ ^3P$ + 11 $4p4d\ ^3P$ + 5 $4s4p^3\ ^3D$
163387.2	161459	1928	2	55 $4s4p^3\ ^1D$ + 35 $4p4d\ ^1D$ + 6 $4s4p^3\ ^3P$
185063.5	184939	124	1	72 $4s4p^3\ ^3S$ + 22 $4s4p^3\ ^1P$
190279.0	190262	17	2	97 $4p4d\ ^3F$
192949.0	192586	363	3	97 $4p4d\ ^3F$
194041.1	194960	−919	1	64 $4s4p^3\ ^1P$ + 24 $4s4p^3\ ^3S$ + 10 $4p4d\ ^1P$
211336.6	211924	−587	2	62 $4p4d\ ^3P$ + 15 $4p4d\ ^3D$ + 9 $4s4p^3\ ^3P$
213932.8	213854	79	1	50 $4p4d\ ^3P$ + 35 $4p4d\ ^3D$ + 7 $4s4p^3\ ^3P$
216420.3	216387	33	0	86 $4p4d\ ^3P$ + 12 $4s4p^3\ ^3P$
216874.5	218779	−1905	2	62 $4p4d\ ^3D$ + 14 $4p4d\ ^1D$ + 8 $4s4p^3\ ^1D$
218746.8	218251	496	1	50 $4p4d\ ^3D$ + 35 $4p4d\ ^3P$ + 7 $4s4p^3\ ^3D$
219381.6	218839	542	3	85 $4p4d\ ^3D$ + 10 $4s4p^3\ ^3D$
219823.3	220259	−436	2	41 $4p4d\ ^1D$ + 24 $4s4p^3\ ^1D$ + 19 $4p4d\ ^3P$
234120.9	233267	854	3	95 $4p4d\ ^1F$
237720.6	237857	−136	1	45 $4p5s\ ^3P$ + 27 $4p5s\ ^1P$ + 22 $4p4d\ ^1P$
238526.0	238229	297	0	97 $4p5s\ ^3P$
240926.0	241845	−919	1	46 $4p4d\ ^1P$ + 42 $4p5s\ ^3P$ + 6 $4s4p^3\ ^1P$
246798.0	246644	154	2	97 $4p5s\ ^3P$
250993.0	250921	72	1	69 $4p5s\ ^1P$ + 16 $4p4d\ ^1P$ + 11 $4p5s\ ^3P$
344908.0	344800	108	2	76 $4p5d\ ^3F$ + 20 $4p5d\ ^1D$
346599.0	346883	−284	3	74 $4p5d\ ^3F$ + 17 $4p5d\ ^3D$ + 8 $4p5d\ ^1F$
346920.0	346966	−46	2	37 $4p5d\ ^3P$ + 31 $4p5d\ ^3D$ + 25 $4p5d\ ^1D$
348555.0	348345	210	1	69 $4p5d\ ^3D$ + 19 $4p5d\ ^3P$ + 11 $4p5d\ ^1P$
352537.0	352653	−116	2	50 $4p5d\ ^1D$ + 22 $4p5d\ ^3D$ + 17 $4p5d\ ^3F$

Table 7. continued.

E_{exp}^a	E_{calc}^b	ΔE	J	Leading components (in %) in LS coupling ^c
353957.0	353722	235	3	75 4p5d ³ D + 21 4p5d ³ F
354291.0	354546	–255	2	52 4p5d ³ P + 43 4p5d ³ D
354795.0	354787	8	0	97 4p5d ³ P
354933.0	354695	238	1	76 4p5d ³ P + 22 4p5d ³ D
358656.0	358908	–252	3	89 4p5d ¹ F + 6 4p5d ³ D
358703.0	358899	–196	0	98 4p6s ³ P
359544.0	359284	260	1	45 4p6s ³ P + 36 4p5d ¹ P + 15 4p6s ¹ P
359571.0	359482	89	1	51 4p5d ¹ P + 29 4p6s ³ P + 10 4p6s ¹ P
366900.0	366837	63	2	99 4p6s ³ P
367959.0	368024	–65	1	75 4p6s ¹ P + 25 4p6s ³ P

^(a) From Saloman (2007) and Rezende et al. (2010).

^(b) This work.

^(c) Only the first three components that are larger than 5% are given.

Table 8. Comparison between available experimental and calculated energy levels in Kr vi. Energies are given in cm^{-1} .

E_{exp}^a	E_{calc}^b	ΔE	J	Leading components (in %) in LS coupling ^c
Odd parity				
0	–1	1	0.5	97 4p ² P
8110	8114	–4	1.5	97 4p ² P
276011	275887	124	1.5	58 4p ³ ² D + 20 4s4p(³ P)4d ² D + 15 4p ³ ⁴ S
278062	277979	83	2.5	73 4p ³ ² D + 25 4s4p(³ P)4d ² D
278787	278812	–25	1.5	81 4p ³ ⁴ S + 13 4p ³ ² D
303697	303768	–71	0.5	81 4p ³ ² P + 12 4s4p(³ P)4d ² P
305385	305317	68	1.5	73 4p ³ ² P + 13 4s4p(³ P)4d ² P
324120	324117	3	0.5	97 5p ² P
326657	326651	6	1.5	97 5p ² P
331956	332334	–378	2.5	62 4s4p(³ P)4d ⁴ P + 32 4s4p(³ P)4d ⁴ D
333133	333229	–96	1.5	63 4s4p(³ P)4d ⁴ D + 34 4s4p(³ P)4d ⁴ P
333936	333776	160	0.5	89 4s4p(³ P)4d ⁴ D + 10 4s4p(³ P)4d ⁴ P
338032	338293	–261	0.5	89 4s4p(³ P)4d ⁴ P + 10 4s4p(³ P)4d ⁴ D
338119	337533	586	3.5	97 4s4p(³ P)4d ⁴ D
338364	338345	19	1.5	63 4s4p(³ P)4d ⁴ P + 35 4s4p(³ P)4d ⁴ D
338447	338128	319	2.5	66 4s4p(³ P)4d ⁴ D + 30 4s4p(³ P)4d ⁴ P
343190	343549	–359	1.5	57 4s4p(³ P)4d ² D + 24 4s4p(¹ P)4d ² D + 14 4p ³ ² D
343505	343767	–262	2.5	52 4s4p(³ P)4d ² D + 23 4s4p(¹ P)4d ² D + 13 4p ³ ² D
352547	351929	618	2.5	50 4s4p(³ P)4d ² F + 38 4s4p(¹ P)4d ² F + 7 4f ² F
359035	359350	–315	3.5	86 4s4p(³ P)4d ² F + 9 4f ² F
374279	374459	–180	1.5	79 4s4p(³ P)4d ² P + 12 4p ³ ² P
377255	377075	180	0.5	83 4s4p(³ P)4d ² P + 10 4p ³ ² P
390595	390620	–25	1.5	47 4s4p(¹ P)4d ² D + 30 4s4p(¹ P)4d ² P + 9 4s4p(³ P)4d ² D
391878	392354	–476	2.5	68 4s4p(¹ P)4d ² D + 16 4s4p(³ P)4d ² D + 11 4p ³ ² D
393018	392851	167	1.5	60 4s4p(¹ P)4d ² P + 19 4s4p(¹ P)4d ² D + 6 4s4p(³ P)4d ² D
394817	393674	1143	1.5	96 4s4p(³ P)5s ⁴ P
399630	398640	990	2.5	100 4s4p(³ P)5s ⁴ P
398678	398754	–76	3.5	43 4s4p(¹ P)4d ² F + 41 4f ² F + 11 4s4p(³ P)4d ² F
399599	399560	39	2.5	43 4s4p(¹ P)4d ² F + 39 4f ² F + 12 4s4p(³ P)4d ² F
403436	404282	–846	0.5	96 4s4p(³ P)5s ² P
408520	409480	–960	1.5	95 4s4p(³ P)5s ² P
442106	441947	159	0.5	88 6p ² P + 11 4s4p(¹ P)5s ² P
443176	443318	–142	1.5	88 6p ² P + 10 4s4p(¹ P)5s ² P
Even parity				
107836	107818	18	0.5	98 4s4p ² ⁴ P
111193	111208	–15	1.5	99 4s4p ² ⁴ P
115479	115484	–5	2.5	98 4s4p ² ⁴ P
141672	141749	–77	1.5	89 4s4p ² ² D + 9 4d ² D
142727	142652	75	2.5	88 4s4p ² ² D + 9 4d ² D
170084	170076	8	0.5	74 4s4p ² ² S + 23 4s4p ² ² P
180339	180370	–31	0.5	74 4s4p ² ² P + 23 4s4p ² ² S
183817	183797	20	1.5	96 4s4p ² ² P
222122	222113	9	1.5	88 4d ² D + 9 4s4p ² ² D
223040	223045	–5	2.5	88 4d ² D + 9 4s4p ² ² D
275380	275380	0	0.5	97 5s ² S
438536	438800	–264	0.5	81 4s4p(³ P)5p ⁴ D + 16 4s4p(³ P)5p ² P
440545	440767	–222	1.5	86 4s4p(³ P)5p ⁴ D + 11 4s4p(³ P)5p ² P
443555	443949	–394	2.5	94 4s4p(³ P)5p ⁴ D
445375	445036	339	1.5	64 4s4p(³ P)5p ² P + 12 4s4p(³ P)5p ⁴ P + 9 4s4p(³ P)5p ⁴ S
445870	444811	1059	0.5	77 4s4p(³ P)5p ² P + 16 4s4p(³ P)5p ⁴ D
447533	447181	352	0.5	95 4s4p(³ P)5p ⁴ P
447950	448161	–211	3.5	97 4s4p(³ P)5p ⁴ D
449512	449240	272	1.5	75 4s4p(³ P)5p ⁴ P + 14 4s4p(³ P)5p ² P + 6 4s4p(³ P)5p ⁴ S
451708	451972	–264	2.5	92 4s4p(³ P)5p ⁴ P

Table 8. continued.

E_{exp}^a	E_{calc}^b	ΔE	J	Leading components (in %) in LS coupling ^c
454259	453858	401	1.5	81 4s4p(³ P)5p ⁴ S + 10 4s4p(³ P)5p ⁴ P + 6 4s4p(³ P)5p ² D
455420	456659	−1239	1.5	87 4s4p(³ P)5p ² D
459761	460313	−552	2.5	92 4s4p(³ P)5p ² D
460752	459393	1359	1.5	64 4p ² (³ P)4d ⁴ F + 32 4s4p(³ P)4f ⁴ F
461201	462268	−1067	3.5	58 4p ² (³ P)4d ⁴ F + 36 4s4p(³ P)4f ⁴ F
469330	468574	756	0.5	95 4s4p(³ P)5p ² S
484507	484069	439	2.5	46 4s4p(³ P)4f ² D + 15 4p ² (¹ D)4d ² D + 11 4s4p(³ P)4f ² F
486270	485581	689	1.5	55 4s4p(³ P)4f ² D + 17 4p ² (¹ D)4d ² D + 12 4p ² (³ P)4d ² D
490658	490863	−205	3.5	51 4s4p(³ P)4f ⁴ F + 32 4p ² (³ P)4d ⁴ F + 5 4s4p(³ P)4f ⁴ D
497145	498729	−1584	3.5	51 4s4p(³ P)4f ⁴ D + 37 4p ² (³ P)4d ⁴ D + 6 4s4p(³ P)4f ⁴ F
502472	501398	1074	3.5	53 4s4p(³ P)4f ² G + 38 4p ² (¹ D)4d ² G + 7 4s4p(¹ P)4f ² G
502548	502755	−207	4.5	54 4s4p(³ P)4f ² G + 33 4p ² (¹ D)4d ² G + 10 4s4p(¹ P)4f ² G
502580	501519	1061	1.5	56 4p ² (³ P)4d ⁴ P + 12 4p ² (¹ D)4d ² D + 9 4s4p(³ P)4f ⁴ D
504083	505060	−977	2.5	39 4p ² (¹ D)4d ² D + 28 4p ² (³ P)4d ⁴ P + 15 4s4p(³ P)4f ² D
504188	504626	−438	1.5	42 4p ² (¹ D)4d ² D + 21 4p ² (³ P)4d ⁴ P + 18 4s4p(³ P)4f ² D
515088	514935	153	0.5	33 4p ² (¹ D)4d ² P + 30 4p ² (³ P)4d ² P + 17 4s4d ² P

^(a) From Saloman (2007) and Farias et al. (2011).

^(b) This work.

^(c) Only the first three components that are larger than 5% are given.

Table 9. Comparison between available experimental and calculated energy levels in Kr VII. Energies are given in cm⁻¹.

E_{exp}^a	E_{calc}^b	ΔE	J	Leading components (in %) in LS coupling ^c
Even parity				
0.0	0	0	0	98 4s ² ¹ S
274931.7	274895	36	0	96 4p ² ³ P
279414.5	279463	-49	1	100 4p ² ³ P
279714.8	279726	-12	2	58 4p ² ¹ D + 32 4p ² ³ P + 10 4s4d ¹ D
288190.2	288165	26	2	68 4p ² ³ P + 27 4p ² ¹ D + 5 4s4d ¹ D
321794.0	321795	-1	0	93 4p ² ¹ S
349973.1	349973	0	1	100 4s4d ³ D
350416.8	350420	-3	2	100 4s4d ³ D
351116.2	351113	3	3	100 4s4d ³ D
379488.3	379488	0	2	83 4s4d ¹ D + 14 4p ² ¹ D
438644.0	438644	0	1	99 4s5s ³ S
447769.0	447769	0	0	98 4s5s ¹ S
578470.0	578470	0	1	98 4s5d ³ D
578722.0	578722	0	2	97 4s5d ³ D
579109.0	579109	0	3	98 4s5d ³ D
581038.0	581038	0	2	95 4s5d ¹ D
616314.0	616314	0	1	99 4s6s ³ S
618693.0	618693	0	0	97 4s6s ¹ S
663983.0	664168	-185	4	39 4p4f ³ F + 25 4p4f ³ G + 24 4p4f ¹ G
664923.0	665371	-448	2	85 4p4f ³ F + 9 4d ² ³ F
664997.0	664462	535	3	51 4p4f ³ G + 31 4p4f ³ F + 14 4p4f ¹ F
671378.0	670779	599	4	44 4p4f ³ F + 34 4p4f ¹ G + 15 4d ² ¹ G
671908.0	672123	-215	3	45 4p4f ³ G + 35 4p4f ¹ F + 18 4p4f ³ F
680086.0	680437	-351	3	89 4p4f ³ D
681681.0	681474	207	2	70 4p4f ³ D + 18 4p4f ¹ D
684070.0	683922	148	1	99 4p4f ³ D
684941.0	685206	-265	2	55 4p4f ¹ D + 26 4p4f ³ D + 17 4d ² ¹ D
694858.0	694912	-54	1	99 4s6d ³ D
695015.0	695051	-36	3	99 4s6d ³ D
695056.0	694966	90	2	99 4s6d ³ D
697330.0	697328	2	2	94 4s6d ¹ D
Odd parity				
117389.6	117398	-8	0	100 4s4p ³ P
120094.8	120083	12	1	99 4s4p ³ P
126553.8	126556	-3	2	100 4s4p ³ P
170835.0	170834	1	1	97 4s4p ¹ P
475890.0	475834	56	2	87 4p4d ³ F + 6 4p4d ¹ D + 6 4s4f ³ F
479655.0	479534	121	3	91 4p4d ³ F + 7 4s4f ³ F
484543.0	484405	138	4	91 4p4d ³ F + 9 4s4f ³ F
487650.0	487948	-298	2	87 4p4d ¹ D + 5 4p4d ³ P + 5 4p4d ³ F
492776.0	492750	26	0	97 4s5p ³ P
493219.0	493247	-28	1	86 4s5p ³ P + 10 4s5p ¹ P
495578.4	495560	18	2	90 4s5p ³ P + 7 4p4d ³ P
497395.0	497387	8	1	83 4s5p ¹ P + 8 4s5p ³ P
501542.0	501700	-158	1	64 4p4d ³ D + 28 4p4d ³ P
501769.0	501895	-126	2	51 4p4d ³ P + 35 4p4d ³ D + 8 4s5p ³ P
505076.0	503287	1789	3	44 4p4d ¹ F + 42 4s4f ¹ F + 13 4p4d ³ D
506933.0	506924	9	0	97 4p4d ³ P
507446.0	507507	-61	1	65 4p4d ³ P + 33 4p4d ³ D
507934.0	508016	-82	2	62 4p4d ³ D + 36 4p4d ³ P
508473.0	508317	156	3	86 4p4d ³ D + 8 4s4f ¹ F + 6 4p4d ¹ F
530349.0	530256	93	2	93 4s4f ³ F + 7 4p4d ³ F
530491.0	530510	-19	3	92 4s4f ³ F + 7 4p4d ³ F
530772.0	530881	-109	4	91 4s4f ³ F + 9 4p4d ³ F

Table 9. continued.

E_{exp}^a	E_{calc}^b	ΔE	J	Leading components (in %) in LS coupling ^c
535462.0	535503	−41	1	94 4p4d ¹ P
560671.0	562201	−1530	3	50 4s4f ¹ F + 47 4p4d ¹ F
587029.0	587029	0	1	84 4p5s ³ P + 14 4p5s ¹ P
594617.0	594617	0	2	99 4p5s ³ P
598281.0	598281	0	1	79 4p5s ¹ P + 15 4p5s ³ P
640160.0	640220	−60	0	100 4s6p ³ P
640761.0	640686	75	1	97 4s6p ³ P
642010.0	642022	−12	2	100 4s6p ³ P
645430.0	645432	−2	1	93 4s6p ¹ P
656725.0	656803	−78	2	99 4s5f ³ F
656868.0	656845	23	3	99 4s5f ³ F
656956.0	656902	54	4	99 4s5f ³ F
659927.0	659904	23	3	96 4s5f ¹ F
719130.0	719730	−600	3	54 4p5d ³ F + 17 4p5d ³ D + 11 4s6f ³ F
724826.0	725290	−464	3	48 4s6f ¹ F + 21 4p5d ¹ F + 15 4s6f ³ F
724718.0	725986	−1268	2	38 4p5d ³ D + 33 4p5d ¹ D + 16 4s6f ³ F
725989.0	724706	1283	4	52 4p5d ³ F + 47 4s6f ³ F

^(a) From Raineri et al. (2014).^(b) This work.^(c) Only the first three components that are larger than 5% are given.

Table 10. Calculated HFR oscillator strengths ($\log gf$) and transition probabilities (gA) in Kr iv. CF is absolute value of the cancellation factor as defined by Cowan (1981). In cols. 3 and 6, e is written for even and o for odd.

Wavelength ^a / Å	Lower level			Upper level			$\log gf$	gA / s ⁻¹	CF
	Energy ^b / cm ⁻¹	Parity	J	Energy ^b / cm ⁻¹	Parity	J			

Table only available via the German Astrophysical Virtual Observatory (GAVO) service TOSS (<http://dc.g-vo.org/TOSS>).

Table 11. Calculated HFR oscillator strengths ($\log gf$) and transition probabilities (gA) in Kr v. CF is absolute value of the cancellation factor as defined by Cowan (1981). In cols. 3 and 6, e is written for even and o for odd.

Wavelength ^a / Å	Lower level			Upper level			$\log gf$	gA / s^{-1}	CF
	Energy ^b / cm^{-1}	Parity	J	Energy ^b / cm^{-1}	Parity	J			

Table only available via the German Astrophysical Virtual Observatory (GAVO) service TOSS (<http://dc.g-vo.org/TOSS>).

Table 12. Calculated HFR oscillator strengths ($\log gf$) and transition probabilities (gA) in Kr VI. CF is absolute value of the cancellation factor as defined by Cowan (1981). In cols. 3 and 6, e is written for even and o for odd.

Wavelength ^a / Å	Lower level			Upper level			$\log gf$	gA / s ⁻¹	CF
	Energy ^b / cm ⁻¹	Parity	J	Energy ^b / cm ⁻¹	Parity	J			

Table only available via the German Astrophysical Virtual Observatory (GAVO) service TOSS (<http://dc.g-vo.org/TOSS>).

Table 13. Calculated HFR oscillator strengths ($\log gf$) and transition probabilities (gA) in Kr VII. CF is absolute value of the cancellation factor as defined by Cowan (1981). In cols. 3 and 6, e is written for even and o for odd.

Wavelength ^a / Å	Lower level			Upper level			$\log gf$	gA / s ⁻¹	CF
	Energy ^b / cm ⁻¹	Parity	J	Energy ^b / cm ⁻¹	Parity	J			

Table only available via the German Astrophysical Virtual Observatory (GAVO) service TOSS (<http://dc.g-vo.org/TOSS>).